High Throughput Exploration of the Oxidation Landscape in High Entropy Alloys

D. Sauceda[a], P. Singh[a,b], G. Ouyang,[b] O. Palasyuk,[b] M. J. Kramer[b], and R. Arroyave [a, c]

[a] Department of Materials Science & Engineering, Texas A&M University, College Station, TX, 77843, USA
[b] Ames Laboratory, United States Department of Energy, Iowa State University, Ames, IA 50011, USA
[c] Department of Mechanical Engineering, Texas A&M University, College Station, TX, 77843, USA

Abstract

High entropy alloys (HEAs) have gained interest for structural applications in extreme environments. With a potentially vast chemical and phase space, there are significant opportunities to discover superior performing alloys. Crucial for most high-temperature applications is understanding and mitigating the oxidation behavior of these chemically complex alloys. Most experimental and computational HEA studies have focused on a limited set of compositions and only a fraction these compositions have been characterized for oxidation. We present a high-throughput framework that utilizes density-functional theory (DFT) in concert with a combined machine-learning model and grand-canonical linear programming for assessing phase stability, phase-fraction, chemical activity and high-temperature survivability of arbitrary HEAs. This framework considers temperature dependent contributions to the Gibbs energy of the competing phases arising from short-range order and vibrational entropy. We demonstrate the effectiveness of the framework by assessing the thermodynamic stability, oxidation behavior, chemical activity, and phase decomposition of body-centered cubic Mo-W-Ta-Ti-Zr refractory HEAs. A total of 51 compositions were analyzed and ranked in order of their survivability based on the Pareto-front analysis. Oxidation was performed at 1373 K on fours samples in air showing the difference in oxidation behavior determined experimentally through scale thickness and their mass changes. The insights on oxidation behavior presented in this work will enable the fast assessment of technologically useful HEAs needed for future structural application in extreme conditions.

Introduction

High-entropy alloy (HEA) design for structural application is exceedingly complex with the difficulty in finding a favorable combination of strength, creep, fatigue, ductility (room temperature), and high temperature corrosion, hydrogen storage, and oxidation resistance for high-temperature applications (1, 2). It was recently found that refractory based HEAs (RHEAs) with typical refractory concentration greater than 50 at.%, have the potential as high-temperature structural materials because of their high-strength, high melting temperature, reasonable toughness and room temperature ductility (3). The exceptional mechanical behavior of HEAs including strength-ductility trade-off, fracture toughness, and

high-temperature strength, resistance to grain growth, and thermal stability have attracted great attention. However, oxidation is one of the critical challenges (4) with chemically complex HEAs needed for applications in extreme environment. The lack of efficient computational tools have made the HEAs hyperspace difficult to evaluate and therefore constitutes a largely underexplored alloy space (5). Although simplified screening tests have been done for determining possible phases present under oxidation conditions (6-8), the oxidation behavior and underlying mechanisms have not been critically assessed.

The high-temperature survivability of an alloy against oxidation is important for many practical applications. Oxidation is a complex process that requires an understanding of phase selection under various P_{O2} and measuring volumetric changes, thermal expansion, and diffusion coefficients and their changes with temperature and time (9-11). Recent studies have summarized critical aspects of HEA formation such as thermodynamics and mechanical behavior (12-16) but we still lack detailed, systematic study on their oxidation behavior. The work by Chen et al. (17) is one such exception, but only a few aspects of high-temperature oxidation were considered. Ellingham diagrams (18, 19) do provide a guide to the possible high temperature oxidation states based on elemental partial pressure and the change in Gibbs formation energy ($\Delta G_{form,T}$) of metal oxides depending on the temperature and composition of the gas phase. Despite being a useful design parameter, no consistent and effective numerical model has been developed capable of analyzing and predicting the interdependencies of the oxidation behavior of complex multi-component systems such as HEAs.

Assessing the phase stability of oxides or intermetallics during oxidation can give key insights about the competing oxide phases and may help design an alloy with higher survivability. However, examination of competition between formation enthalpic forces and the favorable "entropy of mixing" of HEAs at elevated temperatures is complex independently. Making considerations for all entropic sources in the form of vibrational, electronic, magnetic, and configurational degrees of freedom further complicates any predictive methods. While initial estimation of configuration entropy is relatively simple (at least to a first approximation), the temperature dependent contributions originating from lattice vibrations is exceedingly expensive to acquire using traditional DFT methods and require numerically demanding quasi-harmonic approximations (QHA) (20).

Additionally, the entropic effect in HEAs can possibly be overridden by short-range order (SRO) at low temperatures, which can dramatically alter an alloy's thermodynamic stability (21-23). Thus, the proposed high-throughput (HTP) framework is designed to include the SRO correction to enthalpy derived from Sundman et al. (24) for bcc lattices. We also consider the significant effect of competing configurational entropy and SRO on HEA phase stability at elevated temperatures. The HTP machine-learning (ML) framework based on SISSO (**S**ure **I**ndependence **S**creening and **S**parsifying **O**perator) approach (25, 26) directly provides lattice contribution to $\Delta G_{form,T}$ and allows quick assessment of

temperature dependent phase stability, chemical activity of elements and oxygen reactivity. The HTP scheme also combines grand-canonical linear programming (GCLP) (27, 28) to assess temperature-dependent $\Delta G_{form,T}$ of reaction products and change in chemical activity of elements during oxidation.

In this work, we focused on optimizing elemental composition using high-throughput finite temperature phase-prediction framework (HTPF) to provide in-depth understanding of phase stability and oxidation behavior of model bcc Mo-W-Ta-Ti-Zr RHEAs. The RHEAs are natural choice for oxidation investigation due to their excellent high temperature mechanical properties and very high melting temperature. The well-known elements that provide passivating oxide scale such as Al/Si/Cr (29-32), are not considered since the focus of this study is to understand the role of individual refractory elements in the oxidation process. Here we will demonstrate the finite-temperature oxidation behavior of several RHEAs by analyzing phase stability of competing oxide/intermetallic phases, phase decomposition reaction, and elemental chemical potential at finite temperature.

The process for selecting the optimal predicted behavior is a decision tree methodology that combines a newly created metric (*Area-Under-Curve*-2, i.e., AUC2) to rank the HEAs based on their survivability with an evolving criterion based on Pilling-Bedworth Ratio (PBR) (33) with a Lack of Monotonicity (LOM) analysis. The HTPF with AUC2, PBR, and LOM metrics presented in this work will be useful to material science community working on design of structural alloys for high-temperature application.

Methodology

The High-Throughput Finite-temperature Phase Prediction Framework **Fig. 1** is an end-to-end control system for optimizing the phase fraction profile such that it minimizes the thermodynamic properties of the solid-solution from an arbitrary reservoir of component elements. Specifically, in this work the components are limited to the Mo-W-Ta-Ti-Zr RHEA constituent elements and an incremental increase in moles of oxygen. Walking through the function structure diagram in Fig. 1 we can define the inner workings of each sub-function and how it coordinates with the larger prediction framework.

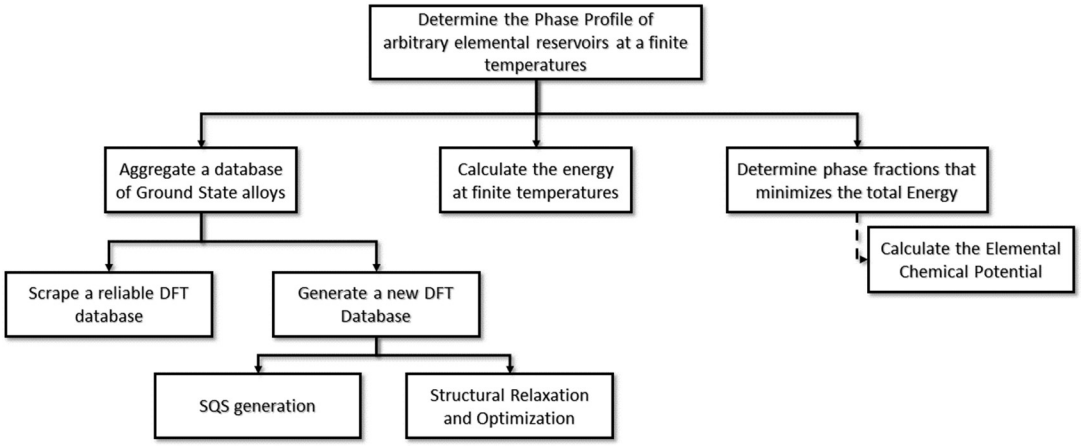

Figure 1. High-Throughput Finite-temperature Phase Prediction Framework that includes three components (i) database generation, (ii) machine-learning model for finite temperature energy assessment (Gibb's formation enthalpy), and (iii) grand canonical linear programming for determining phase-fraction and chemical potential.

Aggregating a Ground-state Alloy Database: A ground-state alloy database consists of two general sources. The first is an established database such as OQMD (34) or materials project (35). The benefit of these databases is to prevent repeating the numerous energy calculations of well-known compositions/structures as well as providing a computational standard for comparative analysis. The second source is user defined database calculated using HTP- DFT workflows. These typically include alloys of interests such as HEAs that are not available in aforementioned databases. In either case, the required features are the total energy, compositions, volume, and formation enthalpy. For this specific work, the OQMD database was chosen for its completeness and acceptance as computational standard (34). However, there are many ordered structures with varying space groups for identical compositions, thus many of the entries are likely unstable or metastable. Therefore, the data is filtered to the unique compositions at the lowest total energy per atom. For the Mo-Ta-Ti-W-Zr + Oxygen phase space, we extracted a total of 202 oxide and intermetallic entries.

*Disorder structure generation and DFT calculation***:** The Alloy Theoretic Automated Toolkit (ATAT) was used to generate special quasi-random structures (SQS) for mimicking disorder on periodic unit cells (36-38). The Mo-W-Ta-Ti-Zr RHEA structures were generated for the compositions in the 10-30 at.% range for each constituent. A schematic SQS for equiatomic MoWTaTiZr RHEA is shown in **Fig. 2**. We must choose a large enough SQS that encompasses all combinations, yet small enough to be reasonable DFT calculations. We found a 50-atom SQS supercell with an acceptable correlation for total of 51 unique RHEAs.

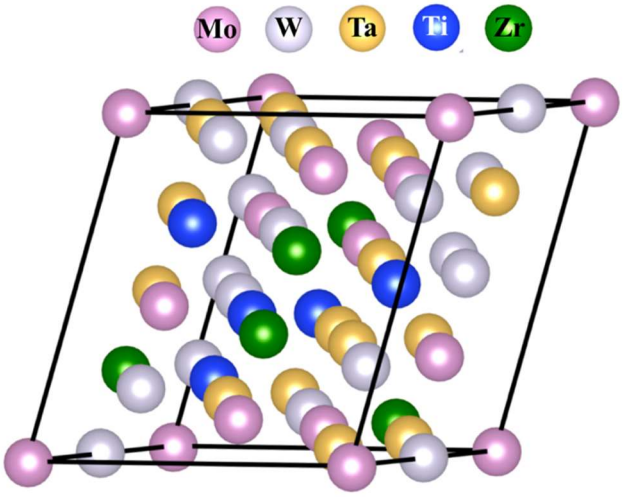

Figure 2. A 50 atom per cell special quasi-random supercell of bcc $Mo_{20}W_{30}Ta_{30}Ti_{10}Zr_{10}$ RHEA.

DFT calculation: The first-principles DFT as implemented in Vienna Ab initio Simulation Package (39-43) and was employed for full relaxation (volume and atomic) and charge self-consistency (total energy and formation enthalpy calculation) of RHEAs. The forces and total energies were converged to 0.001 eV/Å and 10^{-5} eV/cell, respectively. The Perdew, Burke and Ernzerhof (PBE) generalized gradient approximation (39) with a planewave cut-off energy of 533 eV was used. The gamma-centered Monkhorst-Pack (4x4x3) k-mesh was used for geometry-optimization and charge self-consistency (44).

Bartel Model for Finite temperature phase stability prediction: Typical DFT methods are limited to ground-state phase determination using 0 K energies. Therefore, it requires an expensive QHA calculation to include the vibrational entropy contribution at finite temperatures. To address this, we used the Bartel's analytical descriptor that was derived using the SISSO (Sure Independence Screening and Sparsifying Operator) machine-learning method. Greater detail to the training and testing can be found in the original work (25). The SISSO approach is a compressed sensing approach for building predictive models based on N-dimensional descriptors (25). Bartel's model includes the physical descriptors of elements composed of inorganic crystalline solids. The standard $\Delta G_{form}(T)$ is modeled as

$$\Delta G_{form,T} = \Delta H_{form,0K} + G^{SISSO,T} - \sum_{i=1}^{N} x_i G_{i,T} \qquad \text{Equation 1}$$

where, ΔH_{form} is the DFT calculated formation enthalpy, and for $\sum_{i=1}^{N} x_i G_{i,T}$, α_i and G_i are the stoichiometric weight and the absolute Gibbs energy of element i in their parent phases, respectively. The difficulty is that $G^{SISSO,T} = G(T) - \Delta H_{form,0K}$ consists of computationally expensive vibrational contribution. Therefore, the analytical SISSO model in Eq. 2 was used to estimate temperature effect.

$$G^{SISSO,T} = (-2.48 \times 10^{-4} \times \ln(V) - 8.94 \times 10^{-5} \times m \times V^{-1}) \times T + 0.181 \times \ln(T) - 0.882 \quad \text{Equation 2}$$

where V, m, and T are Volume, reduced atomic mass (m), and temperature (T), respectively. The volume is the only DFT generated parameter in Eq. 2, which is simpler than explicitly calculating the vibration entropy using DFT methods within the Quase-Harmonic Approximation (QHA), for example.

The DFT formation enthalpies at 0 K were used in our framework. For clarity, the formation enthalpies at 0K and 298K are not that different. In many cases, RT is at or below the Debye temperature of many compounds and thus vibrational contributions (to the enthalpy) are not likely to be significant, maybe just a fraction of kJ/mol. Another reason for this is the cancellation of effects: compounds and elements may have different temperature dependences in their enthalpies that end up cancelling out. Over ~1,000 K, the enthalpy of formation are not expected to change by more than ~1 kJ/mol (45).

Phase fraction and chemical potential determination – grand canonical linear programming (GCLP): The final component of the framework is a two-step process that helps determining the final details, i.e., phase fractions and chemical potential. First, we determine the optimal phase fraction each available alloy that minimize the energy from the available elemental reservoir (i.e., stoichiometric conservation) by solving the following constrained linear equation:

$$\min_x c^T x \quad \text{s.}t \quad Ax = B \quad \text{Equation 3}$$

which otherwise appears as

$$\min_x E^T_{[alloys_m,1]} \cdot f_{[1,alloys_m]} \quad \text{s.}t \quad Ratio_{[ele_n,allo\ \ m]} \cdot f_{[1,alloys]} == \vec{r} \quad \text{Equation 4}$$

At each temperature and oxygen content a unique profile of phases and fractions are determined. From this information we can then solve the canonical Chemical Potential formula (46).

$$\mu_i = \left(\frac{\partial U}{\partial N_i}\right) \quad \text{Equation 5}$$

Arranging the equation to fit a standard linear equation $A\vec{x} = \vec{b}$ In terms of thermodynamic constants, solving the chemical potential with a linear solver with the form:

$$N \cdot \vec{\mu} = \vec{U} \quad \text{Equation 6}$$

Which is populated like the following.

$$\begin{matrix} TaMo \\ TaW_3 \\ Ti_2O \\ TaMo_2W \\ \vdots \\ HEA\ 0 \end{matrix} \begin{bmatrix} 1 & 0 & 1 & 0 & 0 & 0 \\ 0 & 0 & 1 & 0 & 3 & 0 \\ 0 & 1 & 0 & 2 & 0 & 0 \\ 2 & 0 & 1 & 0 & 1 & 0 \\ \vdots & \vdots & \vdots & \vdots & \vdots & \vdots \\ 10 & 0 & 10 & 10 & 10 & 10 \end{bmatrix} \cdot \begin{bmatrix} \mu_{\mathrm{Mo}} \\ \mu_{\mathrm{O}} \\ \mu_{\mathrm{Ta}} \\ \mu_{\mathrm{Ti}} \\ \mu_{\mathrm{W}} \\ \mu_{\mathrm{Zr}} \end{bmatrix} = \begin{bmatrix} -11.54 \\ -12.50 \\ -8.62 \\ -11.76 \\ \vdots \\ -10.39 \end{bmatrix} \quad \text{Equation 7}$$

The resulting $\vec{\boldsymbol{\mu}}$ is the chemical potential of each element that stabilizes a given thermodynamic equilibrium state.

Finite temperature short-range order contribution to the free energy of HEAs: The long-range order in alloys can be described by occupation of atoms at different sublattices. The same atom in disorder alloys can simultaneously occupy sublattice with different crystal symmetry, which can lead to local ordering, i.e., SRO. The finite temperature processing of most alloys makes inherent SRO contribution highly probable, which is challenging to calculate. We used the two-sublattice model theory of Andersson et al (47) to estimate the SRO contribution in bcc Mo-W-Ta-Ti-Zr HEAs. The Gibbs' free energy of bcc solid-solution phases of RHEA including SRO can be written as:

$$G_m^{\varphi} = \sum_{i=Mo,W,Ta,Ti,Zr} c_i G_i^{\varphi} + RT \sum_{i=Mo,W,Ta,Ti,Zr} c_i \ln c_i + G_m^{E,\varphi} \quad \text{Equation 8}$$

here, G_i^{φ} is the Gibbs formation enthalpy and $c_i \ln c_i$ is point-entropy (c_i is the composition of i^{th} element). The 3rd term $G_m^{E,\varphi}$ is the excess Gibbs' formation enthalpy due to SRO, which can be written as

$$G_m^{E,\varphi} = \sum_{i \neq j} c_i(1) c_j(2).\,[G_o(0K)/(zRT)] \quad \text{Equation 9}$$

where $G_o(0K)$ is the Gibbs formation enthalpy of disorder phase at 0K for given composition, z is number of nearest neighbors for bcc (14, 1st (8) + 2nd (6) nearest neighbors), R is gas constant, T is temperature, and $c_i(1)/c_j(2)$ are the elemental compositions on two bcc sublattices.

Pilling-Bedford Ratio (PBR) Evolution and Lack of Monotonicity (LOM): A direct consequence of finite-temperatures and oxidation exposure to metal alloys are oxidation barriers. However, the formation of oxide phases results in the generation of stresses that can induce cracking or spallation, weakening any protective quality the oxidation barrier may have provided and resulting base metal deterioration. As oxygen diffuses inward through a material, new oxides form at the oxide/metal interface. The molar volume of these new oxides is typically different than those than the substrate. This is captured using the Pilling-Bedworth ratio (33),

Equation 10

$$PBR = \frac{V_{oxide}}{n \cdot V_{metal}} = \frac{M_{oxide} \cdot \rho_{metal}}{n \cdot M_{metal} \cdot \rho_{oxide}}$$ Equation 10

As increasing amounts of oxygen are made available, the profile and fractional amount of oxide and intermetallic components evolve and increase creating an ever-growing volume differential between the oxide scales and the substrate. Ideally, this PBR change should be a smooth monotonic curve that falls between 1 and 2. To evaluate the quality of the PBR evolution we use a normalized Lack of Monotonicity metric described with the following equations (48):

$$LOI_y^*(g) = \frac{\int_0^y (g')^- d\lambda}{\int_0^y |g'| d\lambda}$$ Equation 11

$$LOD_y^*(g) = \frac{\int_0^y (g')^+ d\lambda}{\int_0^y |g'| d\lambda}$$ Equation 12

$$LOM_y^*(g) = 2\min\{LOI_y^*(g), LOD_y^*(g)\}$$ Equation 13

Where $(g')^+$ and $(g')^-$ are equal to $\max\{g', 0\}$ and $\max\{-g', 0\}$ respectively. Lack of Increasingness (LOI) indexes line segment values with $LOI_y^*(g) = 0$ when g is non-decreasing (desired) and larger values when g is farther from non-decreasing. Inversely, LOD or Lack of Decreasingness sets $LOD_y^*(g) = 0$ when the function g is non-increasing and greater values when the function g moves farther from non-increasing. Substituting the g function with a discrete set of PBR points, we conjecture that a non-monotonic function severely hampers oxidation resistance performance.

Experimental method: Four selected RHEA (denoted HEA11, HEA15, HEA45, and C$\overline{10}$) were synthesized by arc melting and then cut into disk shape samples for oxidation tests to validate our theoretical prediction. The sample disks are polished down to 1200 grit sample paper to remove surface defects from the cutting prior to oxidation. The oxidation is conducted in a static air tube furnace that was kept at 1373 K. The samples were introduced to the preheated furnace and were removed from the furnace after 1 hour of exposure and then cooled in ambient air.

Results and Discussion

The order in which each component utilizes, or exchanges information in **Fig. 1** is assembled as a high throughput framework (HTPF). The parameters of the framework are outlined in the method section. The algorithm outlined in **Algorithm 1** defines the connection of the RHEA USER database decomposition prediction with the phase stability predictor, energy minimizer and GCLP solver, resulting in a RHEA decomposition prediction.

Algorithm 1. The algorithm decomposing a RHEA reservoir as function of temperature and oxygen.

Input	:	**Set** *reservoir composition* $\rightarrow \vec{C}$ = Mo: C1, Ta: C2, Ti: C3, W: C4, Zr: C5
Output	:	*RHEA Prediction Object*
Step 1	:	**Run** Bartel Prediction of *OQMD* ***for*** *T = 300, 400, …, 2000K*
Step 2	:	**Run** Bartel Prediction of *HEA* ***for*** *T = 300, 400, …, 2000K*
Step 3	:	**for** *temperature T = 300, 400, …, 2000K*
Step 4	:	**for** *oxygen moles* O = 0, .25, …, 100
Step 5	:	**Append** *O* ***to*** $\vec{C}$
Step 6	:	**Initialize** GEM = GCLP + Energy Minimizer **with**
|	:	Bartel Prediction of *OQMD*
|	:	Bartel Prediction of *HEA*
Step 7	:	**Predict** *phase fraction* **from** GEM **with** $\vec{C}$ **at** T
Step 8	:	**Calculate** *Chemical Potential* **from** GEM *phase fraction*
Step 9	:	**Store** *Phase Fraction*, *Chemical Potential* ***in R****HEA Prediction Object*

Algorithm 1 first requires the input of composition in terms of number of atoms for each element. To implement these two items, the reservoir of elements that can form a solid solution and the particular RHEA composition was investigated. In practice, the investigated RHEA chosen first and then its composition is set to be the reservoir. Step 1 and 2 are the phase stability predictor that uses Mo-Ta-Ti-W-Zr database. The HEA database in this framework is limited to a single entry. Step 3 and 4 are the varying T and O_2 concentration. Step 5 modifies the concentration reservoir with an additional element, which includes oxygen and the effect of expanding composition space to narrow down alloy selections from the database. Step 6 initializes the GEM predictor with input from step 1 and 2. Generally, it combines the databases into a single workable datatype. Step 7 is the (free) energy minimization step that determines the phases present at a given T corresponding to an equilibrium state. The output of this algorithm is a 1-D vector of resulting phase fractions which corresponds to the length of the combined RHEA and OQMD databases. Step 8 is a postprocessing section that uses phase fraction vector from step 7 and calculates change in elemental chemical potential with T and O_2. Step 9 stores results from each T and O_2 iteration into a master predictor for later manipulation. While the algorithm is only defined as a one-step predictor, an additional *for-loop* over the space or set of varying reservoir concentrations (equivalent to the RHEA composition being investigated) can be applied to scan the whole RHEA landscape as shown in **Error! Reference source not found.**.

Algorithm 2. Algorithm decomposing a set of RHEA reservoirs as function of Oxygen and Temperature.		
Input	:	Set *reservoir composition space* → $\vec{S}$ = { $\vec{C_1}$, $\vec{C_2}$, $\vec{C_3}$, $\vec{C_4}$... $\vec{C_n}$ }
Output	:	*RHEA Prediction Object List*
Step 1	:	**for** composition $\vec{C}$ = $\vec{C_1}$, $\vec{C_2}$, $\vec{C_3}$, $\vec{C_4}$... $\vec{C_n}$
Step 4	:	**Algorithm 1**: Predict Decomposition of $\vec{C}$
Step 5	:	Store *RHEA Prediction Object in RHEA Prediction Object List*

Gibbs's formation enthalpy prediction of oxide phases, intermetallic and HEAs: The algorithmically developed framework was employed for analyzing the phase stability and phase fraction profile of RHEAs at elevated temperatures with varying oxygen content. The $\Delta G_{form,T}$ was assessed for 202 oxides and intermetallic phases related to constituent elements of Mo-Ta-Ti-W-Zr-O RHEAs from RT to 2000 K. The heatmap in **Fig. 3** illustrates the $\Delta G_{form,T}$ values on a color scale where positive $\Delta G_{form,T}$ (>0; red) shows energy instability and negative $\Delta G_{form,T}$ (<0; blue) shows stability of given alloy. Consider that well-known oxide phases such as Zr-O or Ti-O compounds and ternary intermetallics such as Zr-Ti-O/Ta-Ti-O/Ti-Mo-O show better stability than RHEAs at elevated temperature. However, phases that include large metals such as Mo/W/Mo-W are energetically less stable. Our analysis provides both quantitative and qualitive detail of the finite-temperature stability of ordered compounds, which will be useful at later stage while analyzing the oxidation behavior. This information will also be useful in general for materials design.

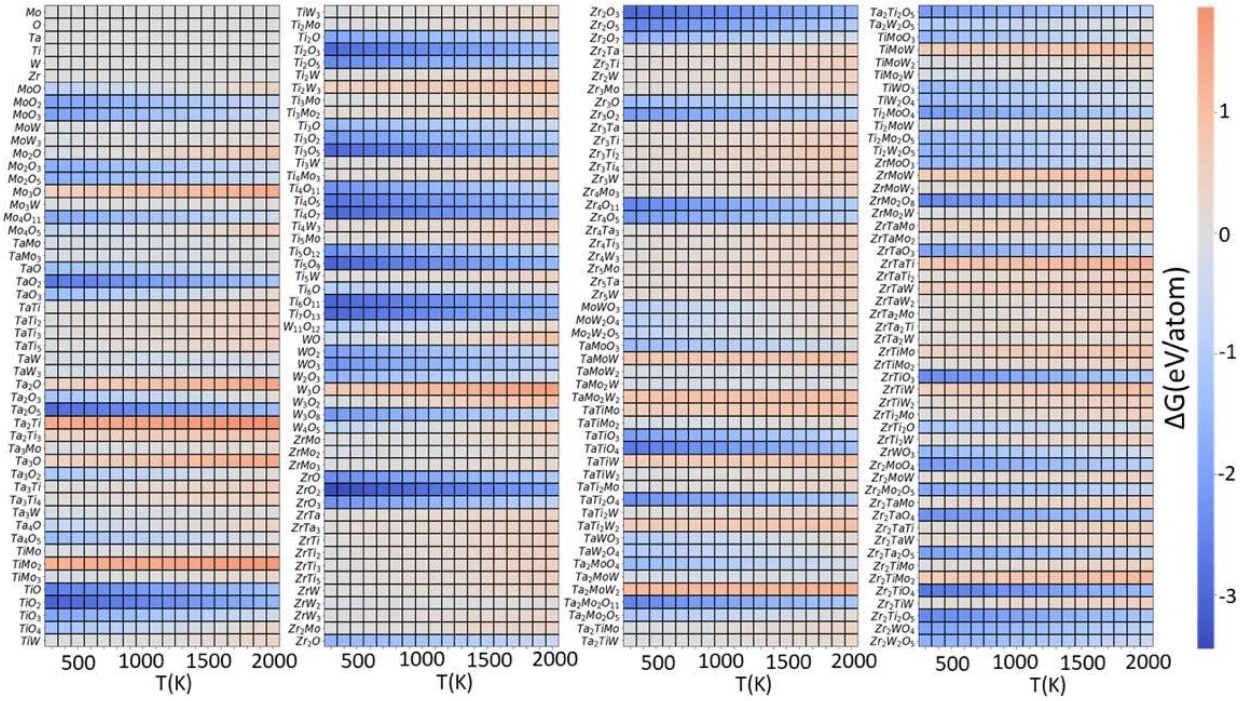

Figure 3: Phase energy predictions of oxides and intermetallic phases of Mo-Ta-Ti-W-Zr HEAs was done using proposed framework in Fig. 1. We have considered a wide temperature range for $\Delta G_{form,\,T}$ from RT to 2000 K, and the alloy phases are sorted alphabetically.

The framework predicted $\Delta G_{form,\,T}$ of HEAs: The knowledge of temperature-dependent $\Delta G_{form,\,T}$ of reaction products during oxidation can greatly help the screening of RHEAs capable of withstanding high temperature oxidizing conditions. The HTPF framework with SRO contribution was used to estimate $\Delta G_{form,\,T}$ of 51 Mo-W-Ta-Ti-Zr RHEAs. The model uses elemental $G_{i,T}$ from experiments and 0 K $\Delta H_{form,\,0K}$ (see supplementary **Table 1**) of RHEAs from DFT to estimate high temperature $\Delta G_{form,\,T}$ as shown in **Fig. 3**. Here x_i is the stoichiometric weight of each element of the compound, $\Delta H_{form,0K}$ is the formation enthalpy; and G^{SISSO} is SISSO predicted entropic contribution to the ΔG_{form} (25). In the top-panel of **Fig. 4**, we can see that small but finite contribution from SRO leads to significant change in trends in $\Delta G_{form,\,T}$. This suggests for the necessity of using temperature dependent corrections to 0 K phase stability in complex alloy systems.

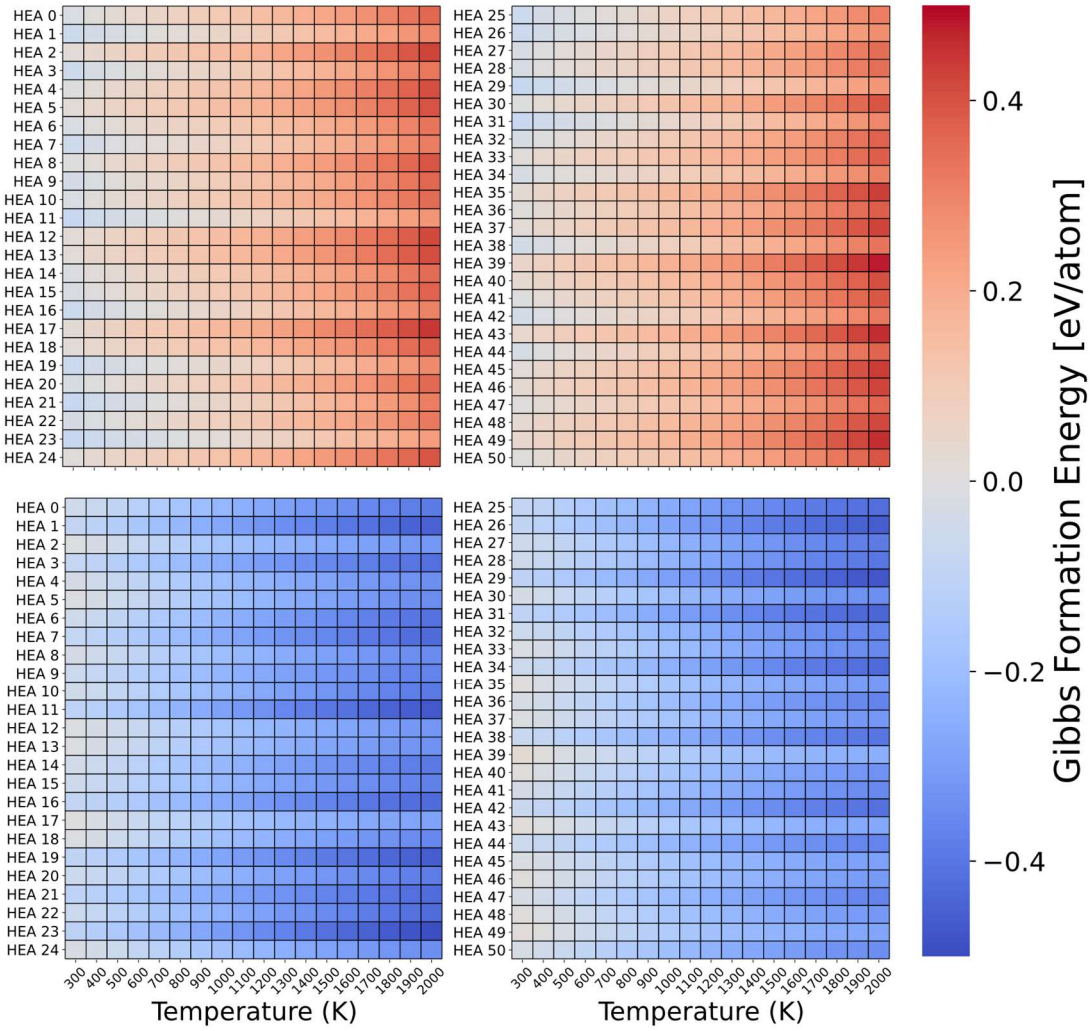

Figure 4. The stability heat map for Mo-W-Ta-Ti-Zr HEAs. The $\Delta G_{form,\,T}$ with (bottom-panel) SRO, and (top-panel) no SRO. The energies are plotted from RT to 2000 K. The actual composition of HEA0-50 and 0 K (DFT) formation enthalpies are provided in the supplement.

We illustrated the components of the G_{SRO} contribution in **supplementary Fig. S1**. As expected, entropy increases with temperature resulting in an increase in SRO contribution to $\Delta H_{form,\,0K}$. Returning to the discussion of **Fig. 4**, the RHEAs become more stable as temperature increases, which is consistent with the $\Delta G_{form,\,T}$ shown in **Fig. 4** (bottom panel). These results are juxtaposed to the OQMD $\Delta G_{form,\,T}$ trend which grows in instability as a function of temperature. Additionally, an example of the RHEA Bartel model prediction without SRO is also included in the supplementary information (see Supplementary Information Document).

Equi-atomic High-Entropy Alloy Results (HEA 0): The implementation of SRO in phase stability analysis strengthens the capability of HTPF framework in **Fig. 1**. Next, we calculated the phase-fraction of possible decomposed phases of RHEAs during oxidation with increasing T and O_2 content. The HEA0 (equi-atomic MoWTaTiZr) was chosen as an example, where HEA0 represents a pseudo baseline in Mo-W-Ta-Ti-Zr RHEA landscape. This section contains the results of HEA0 passed through the steps shown in **Algorithm 1**. First is the assertion that a stochiometric reservoir exists of Mo=20, Ta=20, Ti=20, W=20, and Zr=20 at.% (or 10 atoms each in unit-cell). Then, we evaluated the Gibbs free energy minimization at discrete temperatures for oxygen mole-fractions from 0 to 110 moles in 0.25 mole increments that results into 480 points. For readability, only a subset of points is used in the heatmap visualizations shown in **Fig. 5** which illustrates the phase fraction profile of phase decomposition during oxidation. This dataset is provided in the SI (

Supplementary Data Collection 1: HEA Phase Fraction Prediction).

Energy minimization of HEA0 and phase-fraction determination during oxidation: The predicted $\Delta G_{form,\,T}$ was used to analyze the RHEA reaction products within GCLP model from RT to 2000 K. The temperature dependence of $\Delta G_{form,T}$ with included SRO effect allows us to more accurately reproduce the experimental conditions. The GCLP minimizes $\Delta G_{form,T}$ using grand-canonical ensemble conditions with respect to molar phase-fractions (27, 28). The possible reaction products are summarized in **Fig. 5** and **Table 1** from RT to 2000 K. The color bar from 0-1 shows the molar percent of each phase.

Each grid is a visual representation of the resulting phase fraction at specific temperature. For instance, the top-leftmost heatmap is evaluated at 300K for the full oxygen range. At each mole-fraction of oxygen, a phase profile is constructed denoting all the phases present and their respective percentage of the solid-solution, represented by the hue. Consider that at zero moles of oxygen at 300 K there is zero amount of HEA0 (noted by the grayed-out box). However, the presence of intermetallics TaMo, ZrW_2, and trace amount of $ZrTi_5$, and pure Zr are predicted. Notice that moving across the heatmap, increasing the oxygen amount has diminishing effect on the stability of the intermetallics in favor of growing oxide phases such as ZrO_2, TiO_2, and WO_3.

Our predictions in **Fig. 5** shows that HEA0 at low temperatures is metastable with respect to oxides and other intermetallic phases. The ZrO_2 is the first oxide phase that forms at the onset of oxidation, which was found energetically most stable, which appears at all T's and O_2 mole-fractions. We also found some trace of Zr at low-T at the initial stage of oxidation, however, it was consumed to maintain Zr supply required for ZrO_2 formation at high-T. The Ti_2O_5 and WO_3 are two other stable phases that appears at higher oxygen content as these particular phases need more oxygen than ZrO_2. Our oxidation analysis in **Fig. 5** suggests that HEA0 is stable from 700 K to 2000 K, however, when it exposed to higher oxygen content

the RHEA completely disintegrates either into some oxide and minor intermetallics. This conclusion is in line with short-comings of RHEAs that suffer from high-temperature oxidation.

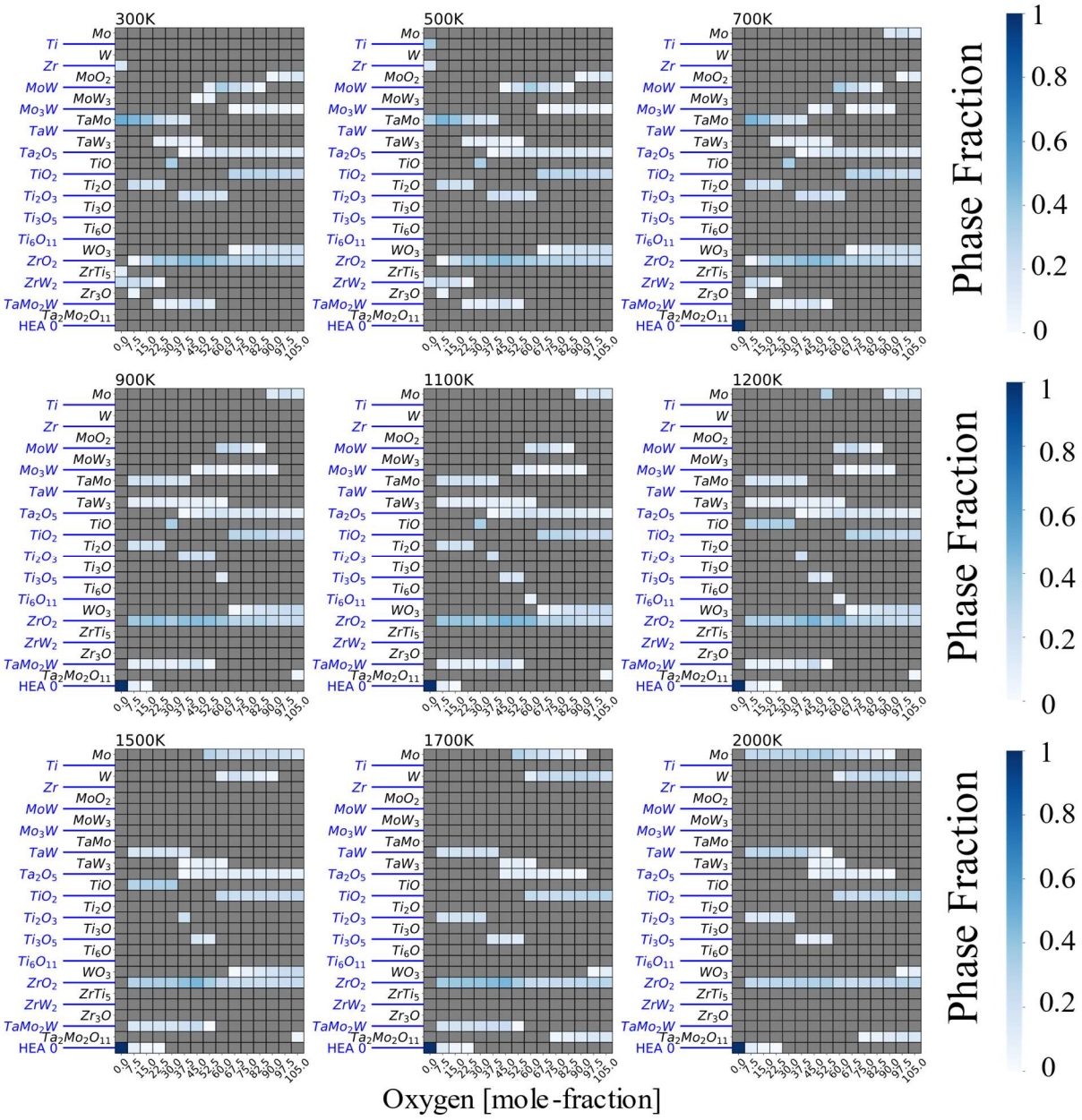

Figure 5. The Phase fraction profile of the HEA0 (equi-atomic MoWTaTiZr). (a-i) Phase fractions of [HEA0 +O_2] reaction products for varying molar percent oxygen in the temperature range RT to 2000 K. The molar oxygen content was varied from 0-105 moles. The dark blue is higher phase fraction and light blue shows lower phase fraction. Blank spots [gray] show absence of specific phase.

The HTPF predicted thermodynamically allowed reaction products during oxidation reaction for HEA0 at 1000 K, 1300 K, and 1500 K and varying oxygen-concentrations are shown in **Table 1**. The

reaction product of x moles of HEA0 (MoWTaTiZr) and y moles of O_2 can qualitatively be written for selective oxidation of Ti as –

$$x.(MoWTaTiZr) + y.O_2 \longrightarrow x.(Mo_{20}W_{20}Ta_{20}Ti_{20-x}Zr_{20}) + y.Ti_2O_5$$

at low temperature or as

$$x.(MoWTaTiZr) + y.O_2 \longrightarrow x.(Mo_{20}W_{20}Ta_{20}Ti_{20-x}Zr_{20}) + y.TiO_2$$

at high enough temperature. Similarly, oxidation of Zr from moderate to high temperature and full oxygen range as

$$x.(Mo_{20}W_{20}Ta_{20}Ti_{20}Zr_{20-x}) + y.ZrO_2.$$

The ZrO_2 was found at all T's and O_2 molar-fractions due to higher chemical activity of Zr. The weaker Zr bonding and hybridization with other transition metals in RHEAs helps increased Zr diffusivity, therefore, enhanced ZrO_2 formation. The ZrO_2 formation results into a Zr depletion in HEA0 substrate at the early-stage oxidation. Similarly, Ti_2O was the other oxide that forms in the presence of low oxygen content, which has the similar origin as Zr due to similar electronic structure. This shows that Ti and Zr are the first oxidizing elements when equiatomic MoWTaTiZr was exposed to static air at elevated temperatures. At higher O_2 concentrations, ZrO_2 oxide scale remains stable, however, Ti_2O transforms to Ti_2O_3 and Ti_2O_5 at medium oxygen exposure while later two transforms to most stable TiO_2 on increased oxygen exposure. The Ti/Zr oxide formation possibly arises from the fact that they have lower partial pressure compared to other alloying elements. The Zr diffusion becomes easier at high-T that helps ZrO_2 to grow further, however, it would be worth checking if the better thermodynamic stability of ZrO_2 and TiO_2 compared to other phases during HEA0 oxidation can stabilize and protect the RHEAs at elevated temperatures.

Analyzing results in **Fig. 5** and **Table 1** shows a couple of key trends in the HEA0 oxidation behavior. The first one is the formation and survivability of the RHEAs. Consider the HEA0 at 700K vs 1200K, both heatmaps show that HEA0 forms at very low oxygen, but under 1200K conditions, the HEA survives oxidation past 22.5 mole-fractions before fully disappearing. Higher temperatures are consistent with experimental fabrication of RHEAs and annealing processes (5). Furthermore, the oxide phases present are the same typical phases observed in during oxidation of RHEAs in experimental condition. After roughly 95 moles of oxygen, the system does not decompose into any new phases, reaching a point of steady state like behavior.

Table 1. Predicted set of thermodynamically favored reaction products in HEA0 (MoWTaTiZr) + O_2 at 1000 K, 1300 K, and 1500 K reaction temperatures. The GCLP minimizes $\Delta G_{form,\,T}$ to predict possible phases and phase-fractions at desired temperature and oxygen concentration.

		Reaction Temperature (K) and Phases-Fractions [For HEA0 + O_2]		
	Mole-Oxygen	1000K	1300K	1500K
I.	0	**HEA 0**	**HEA 0**	**HEA 0**
I.	1	HEA0 + $TaMo_2W$ + **ZrO_2** + **Ti_2O** + TaW_3 + TaMo	HEA0 + $TaMo_2W$ + **ZrO_2** + **TiO** + TaW	HEA0 + $TaMo_2W$ + **ZrO_2** + **TiO** + TaW
II.	25	$TaMo_2W$ + **ZrO_2** + **Ti_2O** + **TiO** + TaW_3 + TaMo	-	-
III.	30	$TaMo_2W$ + **ZrO_2** + **TiO** + TaW_3 + TaMo	$TaMo_2W$ + **ZrO_2** + **TiO** + TaW	$TaMo_2W$ + **ZrO_2** + **TiO** + TaW
IV.	35	$TaMo_2W$ + **ZrO_2** + **Ti_2O_3** + **Ta_2O_5** + TaW_3 + TaMo	$TaMo_2W$ + **ZrO_2** + **Ti_2O_3** + **Ta_2O_5** + TaW_3 + TaW	$TaMo_2W$ + **ZrO_2** + **Ti_2O_3** + **Ta_2O_5** + TaW_3 + TaW
V.	45	$TaMo_2W$ + **ZrO_2** + **Ti_3O_5** + **Ta_2O_5** + TaW_3 + Mo_3	$TaMo_2W$ + **ZrO_2** + **Ti_3O_5** + **Ta_2O_5** + TaW_3 + Mo	$TaMo_2W$ + **ZrO_2** + **Ti_3O_5** + Ta_2O_5 + TaW_3 + Mo
VI	56	**ZrO_2** + **Ti_3O_5** + **Ta_2O_5** + TaW_3 + Mo_3W + Mo	**ZrO_2** + **Ti_6O_{11}** + **Ta_2O_5** + TaW_3 + Mo_3W + Mo	**ZrO_2** + Ti_6O_{11} + **TiO_2** + **Ta_2O_5** + TaW_3 + Mo
VII	65	**ZrO_2** + WO_3 + **TiO_2** + **Ta_2O_5** + Mo_3W + Mo	**ZrO_2** + WO_3 + **TiO_2** + **Ta_2O_5** + Mo_3W + MoW	**ZrO_2** + WO_3 + **TiO_2** + **Ta_2O_5** + W + Mo
VIII.	85	**ZrO_2** + WO_3 + **TiO_2** + **Ta_2O_5** + Mo_3W + Mo	**ZrO_2** + WO_3 + **TiO_2** + **Ta_2O_5** + Mo_3W + Mo	**ZrO_2** + WO_3 + **TiO_2** + **Ta_2O_5** + W + Mo
IX	95	$Ta_2Mo_2O_{11}$ + **ZrO_2** + WO_3 + **TiO_2** + **Ta_2O_5** + Mo	$Ta_2Mo_2O_{11}$ + **ZrO_2** + WO_3 + **TiO_2** + **Ta_2O_5** + Mo	$Ta_2Mo_2O_{11}$ + **ZrO_2** + WO_3 + **TiO_2** + **Ta_2O_5** + Mo

Chemical activity of elements in HEA0 (equiatomic MoWTaTiZr): From the previously determined phases, the chemical potentials can be calculated by minimizing $\Delta G_{form,T}$ from RT to 2000 K using GCLP as described in **Algorithm 1**. The grided subplots in **Fig. 6** illustrate the chemical potentials of the constituent elements. Generally, the refractory elements have varying rates of falling chemical potentials, while oxygen chemical potentials trend upwards. This is consistent with oxidation behavior, as oxygen content increases, there is more opportunity for new oxide phases that serve to reduce the total energy of the solid solution (49). The reaction chain in **Table 1** is associated with the increase in the oxygen chemical potential while the alloying elements show decreasing trends with increasing oxygen molar fractions. Ta shows the highest

chemical activity among all the elements at higher exposure to static air, which can be attributed to its higher partial pressure. Based on elemental chemical activities, three zones were identified in **Fig. 6** namely (i) 0 – 30, (ii) 30 – 65, and (iii) > 60 oxygen molar fractions. There are many other chemical changes during oxidation, however, the three chemical activity zones are mainly attribute to Ti-O phase transformation from Ti_2O to Ti_2O_3 & Ti_2O_5 to TiO_2.

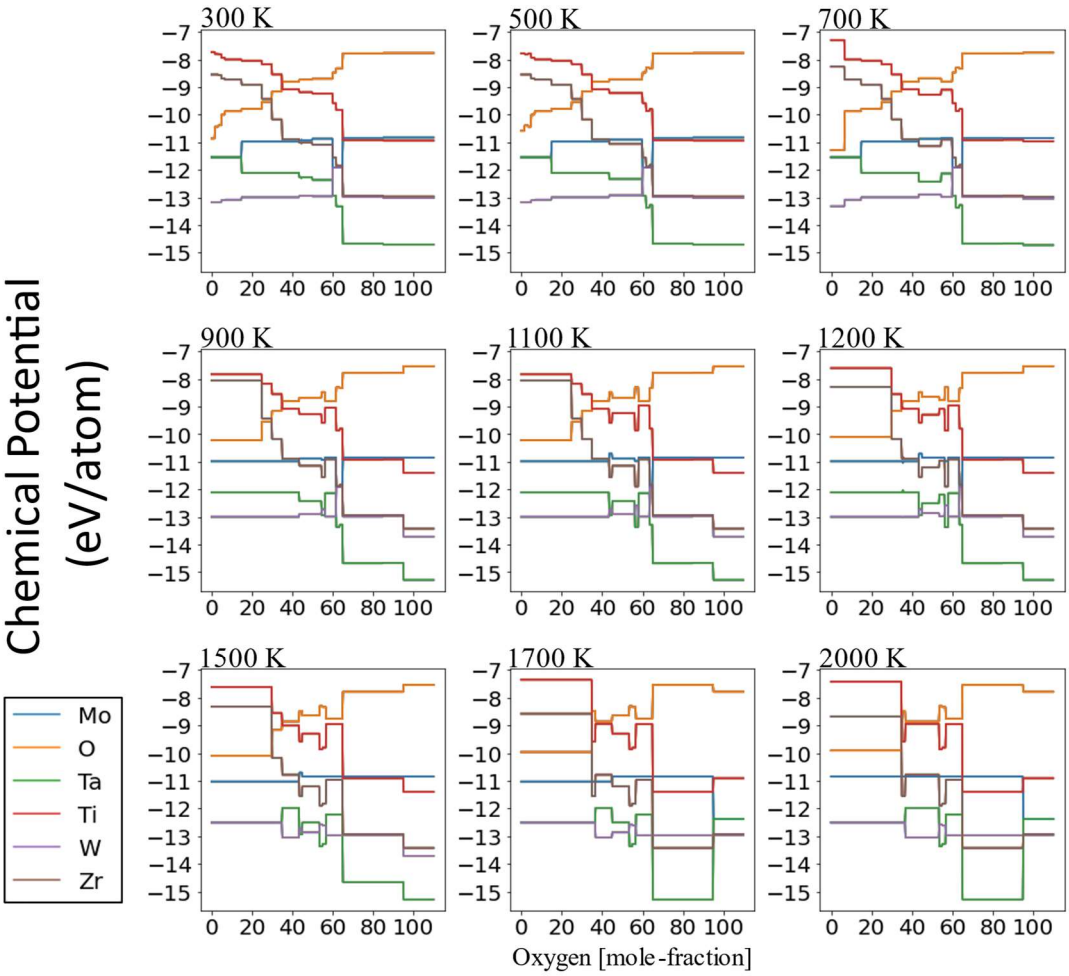

Figure 6. The chemical potential of HEA0 as a function of oxygen mole fractions from RT to 2000 K. The jumps in chemical potential comes from phase decomposition of RHEAs into oxides and/or intermetallic phases.

Each of the curve in **Fig. 7a** shows the effect of oxygen exposure on the total solution energy at varying temperatures. After the energy minimization step has been completed, the final phase profile and their specific phase fractions can be used to minimize the energy using the relation in **Eq. 4**. As oxygen is steadily added to the system, the formation of new oxide/intermetallic phase allows for the system to further lower its energy. Conversely, the increase in temperature leads to increase of the systems energy. For 20-

80 oxygen mole fractions, the chemical potentials are a mix of jump discontinuities and stable plateaus, which can result from a number of possible oxidation behaviors, numerical artifacts, or prediction errors. Strictly looking at the phase evolution behavior, the formation of intermediate oxide phases between stable oxides such as the Magnéli phases (Ti_xO_y or Ti-O) as shown in **Fig. 7b**. A similar observation was also observed in certain non-oxide intermetallics, although they are not as universal as Ti_xO_y.

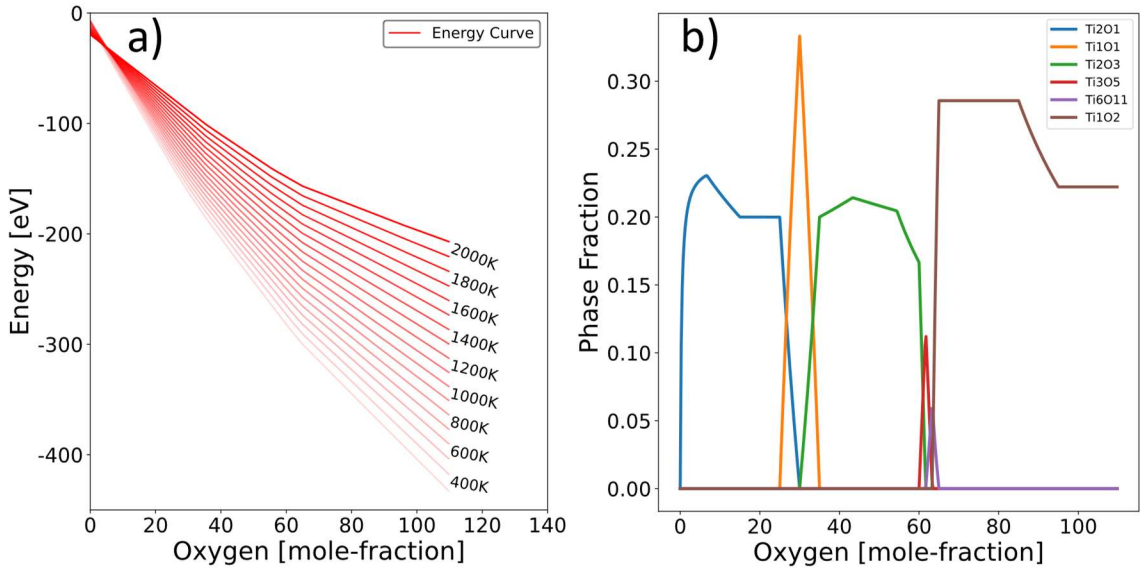

Figure 7. (a) The energy minimization of HEA0 was done by mixing energies of all competing phases in order of their phase-fractions from RT to 2000 K at varying oxygen molar fractions. (b) The phase evolution of Magnéli or Rutile phases (Ti-O) at intermediate phases in HEA0 at 700K.

Aggregated High-Entropy Alloy Results (HEA 0-50): In addition to the individual RHEA predictions, we used the aggregated results of RHEAs defined in **Supplementary Table 1** to interpret their behaviors. By isolating only the RHEA information from each prediction and aggregating respective phase fractions, we analyzed our observations into the comparative survivability against oxidation. Additionally, the phase fraction information beyond max(oxygen) does not remove any RHEAs, which increases the resolution of RHEA deterioration. The comparisons are shown in **Fig. 8**.

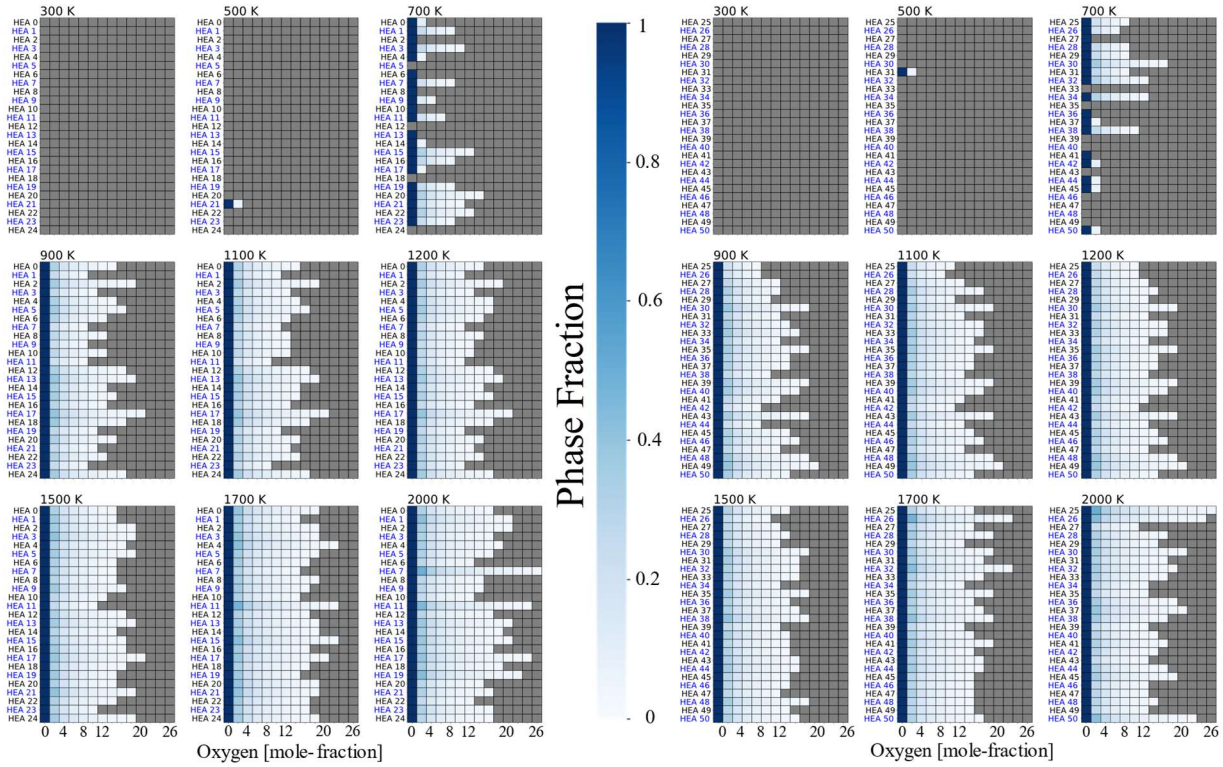

Figure 8. The phase-fraction evolution with oxygen moles for HEA0-HEA50 from RT to 2000 K.

A few observations made from the aggregated AUC2 analysis - (i) HEA31 and HEA21 have the largest solid-solution temperature range, which goes from high-T to 500 K, (ii) HEA7 and HEA25 show the peak survivability during oxidation, and (iii) each of the RHEAs generally increase in survivability as temperature increases to 1900 K. By taking the difference in the survivability from each temperature to the previous temperature, a rate of survivability change is determined. By taking the sign of the survivability change and counting, these RHEA entries experience an improved oxidation behavior, which is the derivative sign of the maximum oxygen per temperature change as shown in **Fig. 9**. As expected, an increase in temperature contributes to the stability of most RHEAs. However, the survivability of RHEAs at 1900K diminishes significantly possibly due to change in relative stability of surviving oxides that are thermodynamically more favorable at higher temperatures. While this does serve to illustrate survivability trends of RHEAs as a function of temperature, it fails to capture the comparative performance.

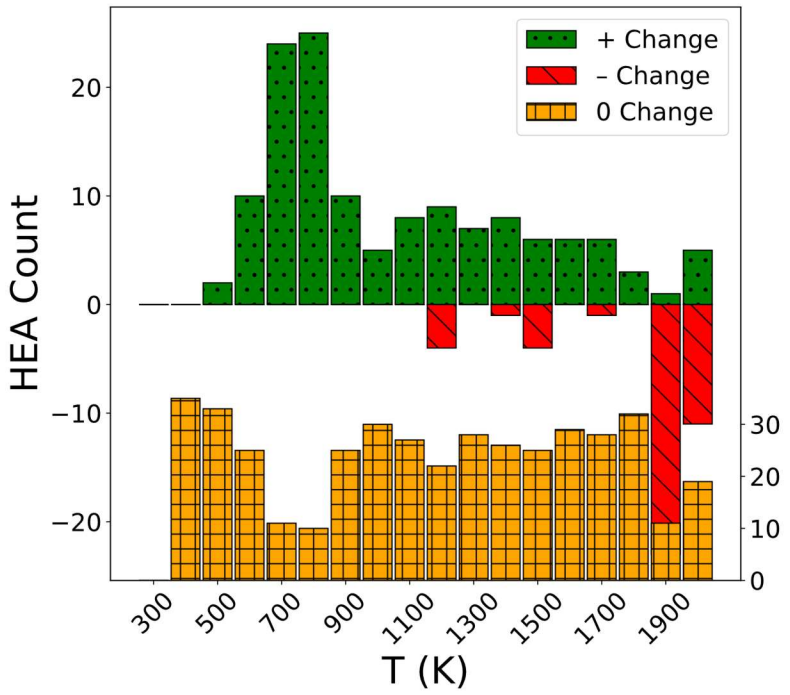

Figure 9. Maximum oxygen survival of RHEAs at given temperature are represented as a negative (red), zero (orange), or positive (green) change in HEA count.

The ideal approach to compare the HEA performance would be to use a rank ordering metric that captures the phase fraction as function of both temperature and oxygen content. Thus, a scoring mechanism, termed double **A**rea-**U**nder-the-**C**urve (AUC2), was created by first evaluating the integral of phase fraction at each temperature over the oxygen space, and then evaluating a second integral over temperature space. **Figure 10** shows a graphical representation of the AUC2 score for HEA0 (equiatomic MoWTaTiZr) from RT to 2000 K. Notice that if AUC2 was evaluated only from 300K-600K, it would be zero since no HEA is formed at any point of oxygen in this temperature range (see **Fig. 5**). In the following sections, our analysis would be based on the AUC2 score, however, it will be worth highlighting some useful considerations when using the proposed approach - (i) AUC2 is a metric based on theoretically predicted phases and their phase fractions formed during oxidation, (ii) in exchange to dimensional reduction of temperature and oxygen dependent phase fractions, there is an inherent loss of localized information. For example, a phase fraction profile that occurs at a 2000K up to 10 moles of oxygen has the same score as an identical phase fraction profile 500K between 30 and 40 moles of oxygen, and (iii) AUC2 should only be used for comparing the survivability of different HEA entries, but not between decomposed phases vs HEAs.

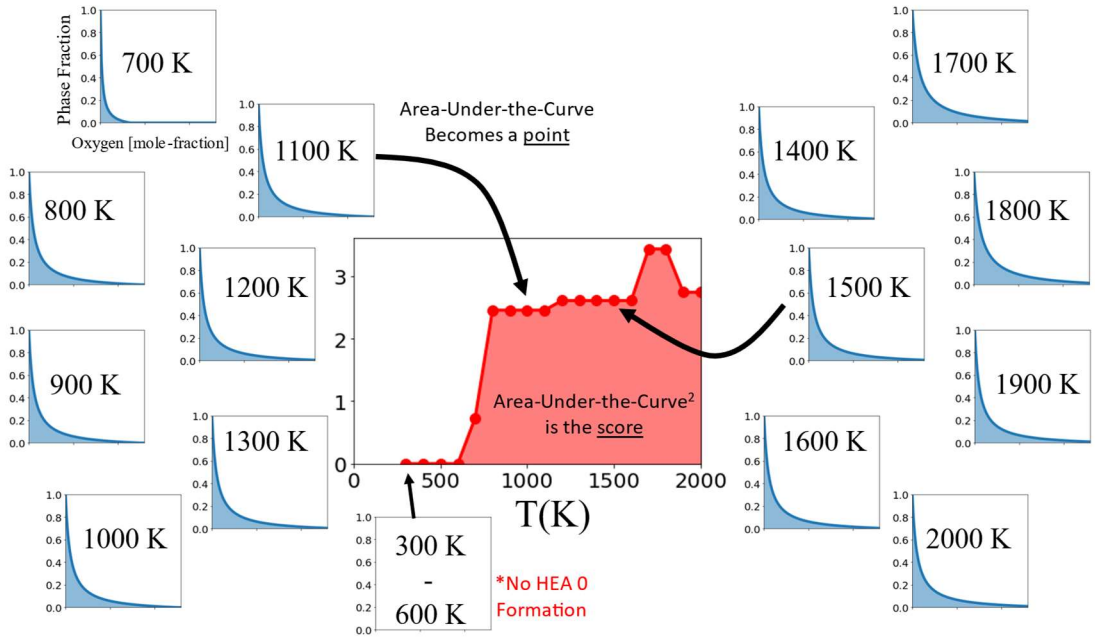

Figure 10. Graphical representation of AUC2 scoring method for RHEAs, which is exemplified for HEA0.

The AUC2 for each of the RHEAs are grouped by their dominating elements. As a result, a number of RHEAs with multiple dominating elements such as HEA30 ($Mo_{30}Ta_{10}Ti_{20}W_{10}Zr_{30}$) that has the same Mo and Zr compositions falls in both categories, see **Supplementary Table 2**. Furthermore, the HEA0 appears in all groups as a pseudo baseline. For comparison, we plot the AUC2 of the sorted RHEAs in **Fig. 11a** with respect to HEA0 showing survivability trends. Some critical observations after sorting of AUC2 suggests that (i) the Ta rich HEAs perform worse than HEA0, (ii) the HEA17 ($Mo_{20}Ta_{10}Ti_{30}W_{10}Zr_{30}$) is the top performing HEAs in the Zr and Ti rich entries, and (iii) HEA30 ($Mo_{30}Ta_{10}Ti_{20}W_{10}Zr_{30}$), a second-best performer alloy, is common in both Zr and Mo rich entries. Although further analysis is required, HEA17 ($Mo_{20}Ta_{10}Ti_{30}W_{10}Zr_{30}$) and HEA30 ($Mo_{30}Ta_{10}Ti_{20}W_{10}Zr_{30}$) are strong candidates for selection due to their higher survivability against oxidation.

To get a better sense of performance trends, we show the strip-point factor plots based on elemental concentration in **Fig. 11b**. The SQS used in DFT calculations consists of 50 atoms per cell of Mo-W-Ta-Ti-Zr RHEAs, where the elemental concentrations were varied in the interval of 10 at.%(i.e., X1=5 atoms). Taking HEA that satisfies a concentration of individual constituent element and plotting AUC2 in the concertation category with coordinating elemental color gives the scatter points in **Fig. 11b**. The mean value and standard deviation are calculated to generate the error bars and connection points between like colors across the composition categories. What the figure shows is not particularly remarkable but does illustrate some slight diminishing AUC2 trends that can be arguably attributed to increasing amounts of Ta and W. Discernable trends are not definitive for other constituent elements as a result of standard deviation

overlap. While the mean trend for 10 and 20 at.% Zr inches upwards, the standard deviation of category 20 at.% almost completely envelopes the standard deviation of category 10 at.%. From the same methodology, we show factorization of AUC2 scores over elemental pairs with nominal RHEA compositions in **Fig. 12**, where the overall trend is convoluted especially in the mid-regions of the figure. However, based on analysis of **Fig. 11b**, we concluded that HEA17 and HEA30 are possibly the stronger contenders for oxidation resistant alloys. One may argue that this a result of high Ti-Zr or Mo-Zr concentrations, where the middle and right regions show consistent improvement in oxidation behavior of RHEAs. This can be concluded with two important observations - (i) the standard deviations are overlapping, casting some qualitative uncertainty similar to **Fig. 11b**, and (ii) the left region does not have constant improvement.

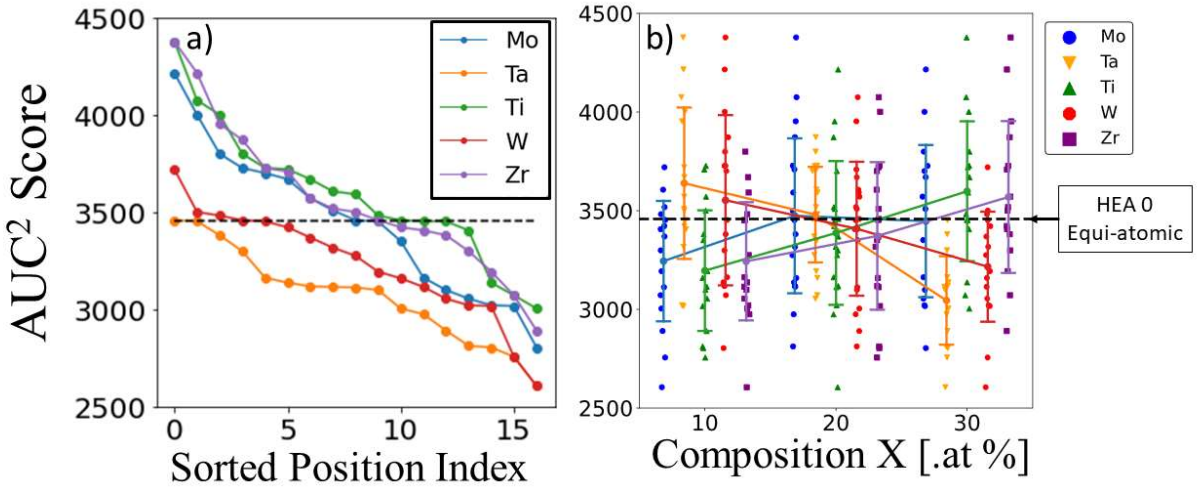

Figure 11. (a) The RHEAs grouped by the presence of elemental compositions (i.e., 15 atoms per cell ~ 30 at.%) that are compared with HEA0 AUC2 baseline. (b) The strip and point plot illustrates the factorization of AUC2 scores over the nominal elemental composition. Each factor is connected by the the mean AUC2 score with std. dev.

The analysis of Ti-Zr (yellow) trends in **Fig. 12** show similar point-strip factor plot in **Fig. 11b**. The standard deviation is significantly larger than **Fig. 11b**, therefore, it is more advantageous to find out elements responsible for diminishing performance to reconcile these issues rather than improving it. Consider the Ta-W (brown) case in **Fig. 12**. Moving from left to right, increasing amounts Ta-W are heavily correlated with worse performing HEAs. The 30 at.% (15 atoms) of both Ta and W predicts a low AUC2 with a narrow standard deviation, and inversely the 10 at.% (5 atoms) pairs are responsible for the highest AUC2 values which result in HEA17, HEA30, and HEA32. Interestingly, HEA15 ($Mo_{20}Ta_{10}Ti_{30}W_{20}Zr_{20}$) is missed from this list since W has 20 at.% (10 atoms) rather than 10 at.% (5 atoms). While seemingly an error, it is actually consistent with the general trends of **Fig. 11b** and the middle region trends of **Fig. 12**.

The resulting conclusion is that while W and Ta are both deleterious to RHEA survivability, Ta has a greater impact. This suggests that in alloy preparation it would be advantageous to minimize both Ta and W at.%.

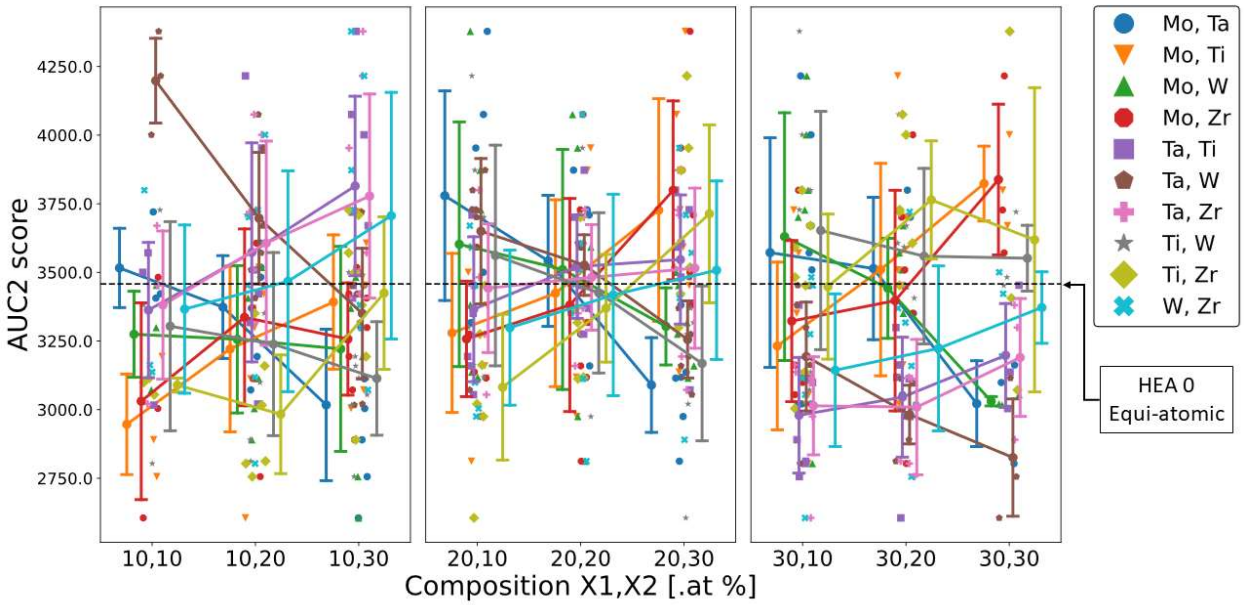

Figure 12. We illustrate the factorization of AUC2 scores over elemental pairs with nominal RHEA compositions. The plot can be decomposed into three region based on concentrations of (X1, X2), where X1=10,20,30 at.%, and X2=10,20,30 at.%. Each metal pair is connected by the the mean AUC2 score, and the error bars are represented by standard deviation.

Competing Phases Pareto Analysis: Thus far, this work has illustrated the components of the prediction framework as well as the predicted phase fractions and chemical potentials produced over a landscape of RHEAs. Furthermore, we have created rudimentary, yet unique metrics for visualizing comparisons between predictions. In a sense, this is a thermodynamic/oxidation behavior catalog of RHEAs. This sequence of analysis is intended to serve as a guide to the experimentalists in synthesizing new alloys with predicted behavior. **Fig. 11&12** provide sufficient level of information for determining materials selection. However, it falls short of what is regarded as "materials design". The AUC2 methodology for HEAs also holds true for oxides and intermetallics that evolve with temperature and oxygen. The heatmap in **Fig. 13** shows the phase decomposition landscape limited to phases that are seen at least once. A more technical information derivation is provided in the supplementary material.

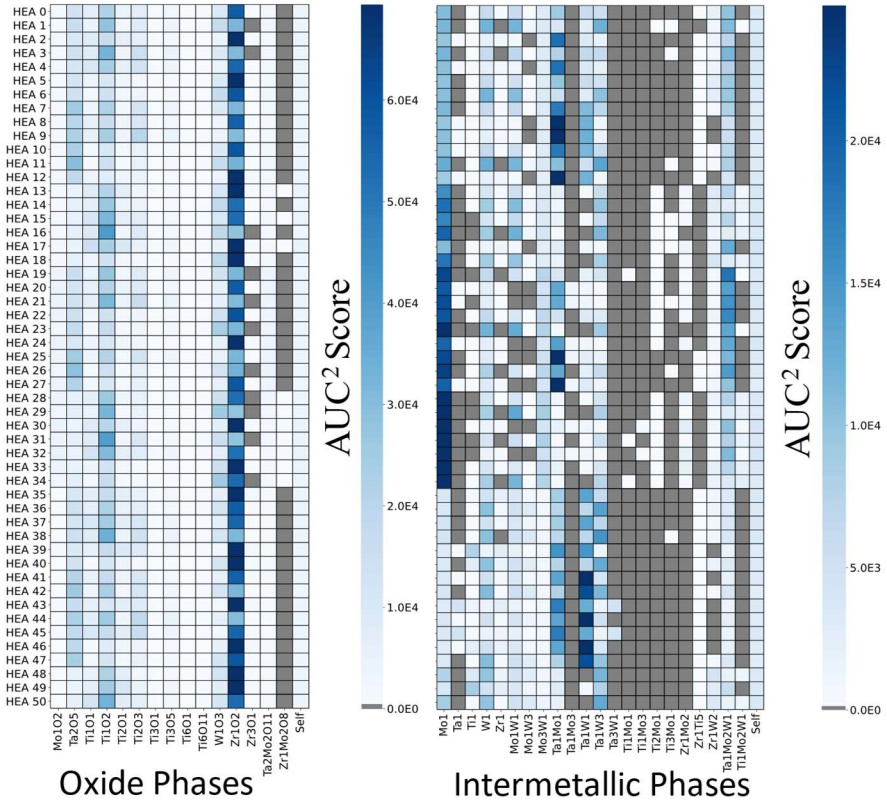

Figure 13. Heatmap of AUC2 scores of all RHEAs (HEA0-50) with respect to (left-panel) oxide, and (right-panel) intermetallic phases. Each row corresponds to a composition reservoir equivalent to a RHEA. The last column in each plot is representative of AUC2 score with "Self", e.g., HEA0 vs HEA0.

Discussion: To compensate for the lack of kinetic considerations, we conduct two additional analyses for an optimal HEA candidate selection. The first is a limited literature review was conducted to study the general behaviors of the oxides found in **Fig. 14**. There does exist a publication bias in the literature towards the discovery and observation of durable HEAs, typically consisting of protective alumina, chromia and, occasionally rutile layers. Given the absence of either alloying elements Al- and Cr- many of the experimental observations cannot be immediately applied to the Mo-Ta-Ti-W-Zr systems. However, occasional HEAs oxidation failures can be found dispersed throughout the studies and give insight into the behavior of a particular oxide phase.

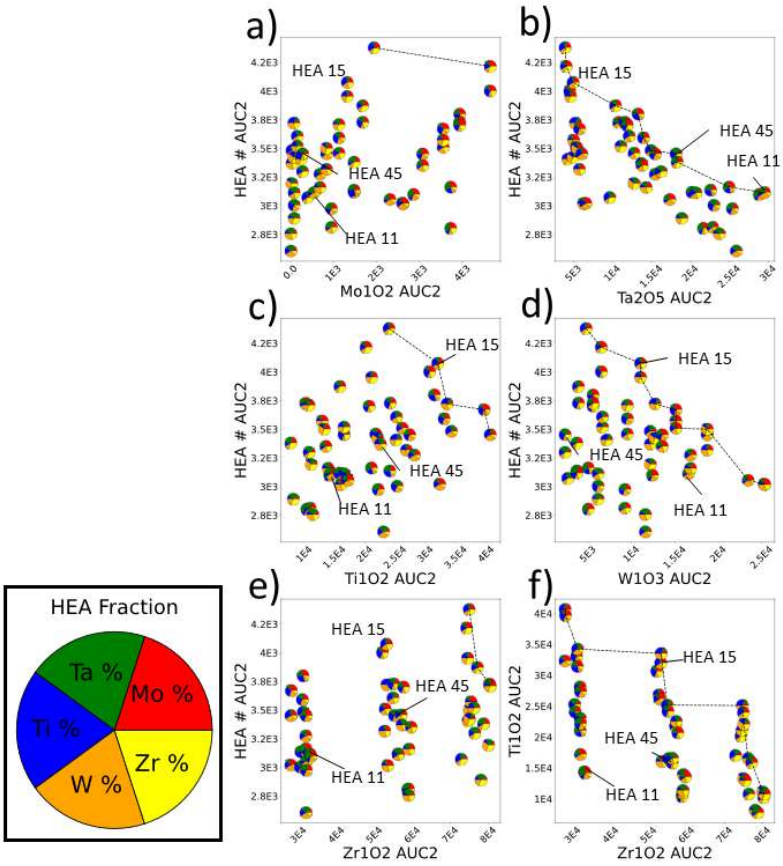

Figure 14. Pareto front analyis of AUC2 scores of RHEAs with respect to (a) MoO_2, (b) Ta_2O_5, (c) TiO_2 (rutile), (d) WO_3, and (e) ZrO_2 . (f) The comparison of AUC2 scores of TiO_2 vs ZrO_2. The HEA labels marked in black are on the pareto front while the red labled are the entires of interest (see the AUC2 sccores in supplementary **Table 1,2**).

From the literature Mo is known to have a much higher oxidation rate and an oxide, MoO_2, with low melting temperature 1068 K. Experiments discussing the alloying effects of Mo however actually result in MoO_3 rather than MoO_2 (50, 51). Given that their respective formation energies are -2.163 eV/atom and -2.155 eV/atom (a difference of only 8 meV/atom), the assumption is that the discrepancy is the result of inherent uncertainty in the Bartel model. The MoO_2 in **Fig. 14a** has a pareto front of HEA17 and HEA30 (connected by dashed line). Chemically, MoO_2 is not a feasible phase during oxidation in Mo based alloys, which was included for completeness during our analysis of all possible phases that can theoretically results from Mo-W-Ta-Ti-Zr based HEAs. Regardless, the fast oxidation and volatility prevents any oxidation protection, permeating the base material and can lead to pores and evaporation however does not cause cracking. For this reason, MoO_2 should be moderately minimized when possible. Ignoring the Pareto front, HEA15 possibly comes out as a good candidate with better oxidation resistance.

The pareto front for Ta_2O_5, shown in **Fig. 14b,** has a downward diagonal trend. This implies that an increased presence of Ta_2O_5 has a direct correlation with diminished HEA formation. As one would expect, increased amounts of Ta yield to form larger amounts of Ta-O, illustrated by the green slice of the scatter pie-charts. This is consistent with the conclusions of **Fig. 11b** and **Fig. 12** that suggest Ta is deleterious to HEA survivability. Experimentally, Ta_2O_5 has a Pilling–Bedworth ratio (PBR) of 2.5 (52) which can lead to stress concentrations within oxide scales (53), causing breakaway oxidation (1). Although it has been suggested that allowing for slow formation of oxidation to relieve the internal stresses, Ta_2O_5 should be avoided as much as possible, i.e., HEA15 is one of the ideal candidates.

Rutile phase, TiO_2, shown in **Fig. 14c** indicates a positive albeit, slight, upward correlation between HEA and TiO_2 formation as seen by the widening blue slices. TiO_2 is well-known to form a protective layer, however it is usually in conjunction with alumina (54). There has been some criticism as to the effectiveness of TiO_2 as an oxidation shielding mechanism as a result of non-uniform scaling (55). However, for optimal selection purposes, if one were faced with the inevitability of oxidation, TiO_2 would serve as a greater benefactor than a hinderance. Realistically, any HEA along the Pareto front would be a reasonable selection. Recalling that kinetic effects are ignored in the predictions, it may be the case that a significantly large region of TiO_2 would overcome the degradation of HEAs as a result of thermodynamic instability at finite temperatures and oxygen content.

Tungsten is often selected for its inherent mechanical properties and irradiation resistance but not for their oxidation performance. There is limited direct examination of WO_3 in the context of HEAs due to its volatility and the general bias in avoiding it all together. Often the effectiveness of a protective oxide layer is discussed in terms of prohibiting WO_3 growth (7). Most conclusions that consider WO_3 formation a negative are inferred from oxidation behaviors of pure tungsten (56) (49) where PBR is 3.3, i.e., volatile and subject to sublimation at higher temperatures. This can lead to cracking, spallation, and/or pesting. This indicates that it may be more beneficial to use an inequality selection rather a pareto for an optimal selection as shown in **Fig. 14d**.

Finally, ZrO_2 in **Fig. 14e** is by far the most stable of the oxide byproducts. With a formation energy of -3.632 eV/atom and left purely to thermodynamic mechanisms, ZrO_2 formation exceeds several times compared to any of the other oxides at equivalent composition. At the initial outset of this work, it was assumed that plentiful ZrO_2 would be a positive for oxidation resistance. However, in work carried Sheikh et al (57) an $Hf_{0.5}Nb_{0.5}Ta_{0.5}Ti_{1.5}Zr$ RHEA was oxidized under a temperature range of 873-1373 K. Although it is a single experimental observation, apart from Hf- and Nb-, the composition is quite analogous to the prediction phase space. The exposure of $Hf_{0.5}Nb_{0.5}Ta_{0.5}Ti_{1.5}Zr$ to oxidation environment from 873-1373 K does not show significant protective oxide layer, therefore, a prolonged exposure leads to catastrophic oxidation and pesting. However, a dramatic shift in oxidation response at 1373 K was observed where no

pesting occurs due to the presence of two distinct oxidation layers composed of simpler oxide phases in complex form, i.e., (Zr, Nb)O_2 and (Ti, Nb)O_2, which form as a result of TiO_2 and ZrO_2 reactions with the base material. Notably, Al and Cr are significant oxidizing agents, when these are included as constituent elements, the kinetics of ZrO_2 and TiO_2 is dwarfed, therefore, it is difficult to observe.

Returning to the predictive framework, the dual oxidation response informs the succinct behavior of ZrO_2. While tetragonal ZrO_2 is a thermodynamically stable barrier layer oxide (58), at sufficiently low temperatures (assumed in range of 873-1373 K) Zr cannot unbind itself from the base RHEA material to form a protective scale. The reactive nature of Zr leads to oxidation deep within the material causing pesting, however, it is not a definite that this will be the case for the Mo-W-Ta-Ti-Zr phase space. Regardless, an optimization towards ZrO_2 should be met with some skepticism. It is difficult to recognize an appropriate criterion for HEA selection, however given the previously discussed oxides, there are a number of repeating players that are a point of interest namely including HEA15.

The **Fig. 13** illustrates AUC2 scores oxides. The ZrO_2 is a stable oxide that gives higher AUC2 values. Other significant phases are rutile (TiO_2), tungsten trioxide (WO_3), and tantalum pentoxide (Ta_2O_5). Although the extreme values of ZrO_2 diminishes the resolution of the other oxide phases, it is still apparent that darker regions of Ta, Ti, and/or W oxides, diminishes the AUC2 score of ZrO_2. This is consistent with our arguments that oxide formation is a zero-sum game at finite oxygen content. The rightmost figure is a similar analysis to the previous one, but only contains intermetallic components that fit within the RHEA phase-space region. From a design perspective, the HEA survivability is important, however, when RHEAs inevitably decompose the question arises - “what are the desired or deleterious oxides and intermetallics that form?”. Thus, we present a Pareto front analysis demonstrated in **Fig. 14e** using the AUC2 scores of both the RHEAs and competing phases.

Each point in the Pareto front is determined by the respective RHEA and ZrO_2 AUC2 scores. To illustrate the compositional trend each point is replaced with a pie chart of fractional elements. The three regions of ZrO_2 and AUC2 scores are roughly 3E4, 6E4, and 8E4 and sensibly correspond to 10%, 20%, and 30% of Zr content in the RHEA in **Fig. 14e**. By repeating this analysis for other significant oxide phases, a grid of pareto fronts can be generated to assist in the composition selection for an ideal RHEA selection as shown in **Fig. 14e**.

Given that group IV elements are known to consume large amount of oxygen (59), **Fig. 14f** illustrates the inherent competition for oxygen content required to form zirconia and rutile. Given that both oxides are key players in the formation of a protective oxide layers, it can be reasoned that HEA15 would provide a reasonable middle ground between the two. Considering the experimental observations for kinetic behavior, the qualitative trends suggests avoiding MoO_2, Ta_2O_5, and WO_3 while targeting TiO_2 and to some extent ZrO_2.

***Experimental validation*:** To evaluate the quality of our prediction, we synthesized and performed oxidation of three RHEAs, and additionally, we included $C\overline{10}$ ($Mo_{80}W_5Ta_5Ti_5Zr_5$) (60) that is known to perform particularly poorly under oxidation conditions. The **Table 2** shows the selected RHEAs with high (HEA45), medium (HEA11), and low/bad ($C\overline{10}$) oxidation survivability based on our predicted AUC2 score, also see **Supplementary Table 1 &2**.

Table 2: The four selected RHEAs for oxidation survivability experiments.

#	HEA [at%]	dH [eV/atom]	V [A³/atom]	E [eV/atom]	AUC²
HEA 45	$Mo_{10}Ta_{30}Ti_{30}W_{10}Zr_{20}$	0.0526	18.215	-9.963	3453
HEA 15	$Mo_{20}Ta_{10}Ti_{30}W_{20}Zr_{20}$	0.0219	17.582	-10.002	4075
HEA 11	$Mo_{20}Ta_{30}Ti_{10}W_{30}Zr_{10}$	-0.0226	17.109	-11.280	3114
$C\overline{10}$	$Mo_{80}W_5Ta_5Ti_5Zr_5$	-0.0531	16.290	-10.792	1228

The HEA compositions show significantly different oxidation behavior (**Fig 15**). The $C\overline{10}$ was completely oxidized turning into mixed crystalline oxides depleted of Mo. Its mass change after the 1-hour exposure was significant, being -300 mg/cm^2. While HEA15 provided better oxidation resistance compared to $C\overline{10}$, it has excess scale growth. Though the scale is porous and not well adhered, it does provide some oxidation resistance blocking rapid oxygen diffusion into the alloy. On the other hand, HEA11 and HEA45 showed slightly enhanced oxidation resistance than HEA15. The oxide scale for both is thinner, and the unit mass change is smaller. A rating for these four compositions for oxidation resistance at this test condition can be listed as HEA45 > HEA11 >> HEA15 >> $C\overline{10}$. Explicitly stated, this does not follow the AUC2 trend, although following the principles of our literature review we will confirm or selection criteria.

In contrast to other oxides present, MoO_3 is highly volatile above 1073 K, and WO_3 starts to sublimate significantly above 1573 K. $C\overline{10}$ consists of 80 at % of Mo (or 69.4 wt %), without any passivating elements. The amount of Mo present in the sample matches with the 68.8% total mass loss observed after the 1-hour oxidation tests, which confirms a nearly total loss of Mo. There may have been some outer Ti, Zr rich outer oxide scale but is likely disrupted by the MoO_3 vapor. Oxides of Ta and W remained throughout the sample and were confirmed our EDS analysis. Compared to $C\overline{10}$, HEA11, HEA15, and HEA45 showed a significant improvement in oxidation resistance, mainly due to their reduced refractory content, especially Mo. HEA11, 15, 45 have enough Ti, Zr to exhibit a distinct layered structure after oxidation, i.e. an outer oxide scale that is porous, a partially oxidized internal oxidation layer, and an unaffected base alloy. The oxides of Zr and Ti are much more stable than that of other refractories. ZrO_2 and Ti_2O_5 form first and are enriched in the outer oxide scale. However, ZrO_2 and Ti_2O_5 are neither compact and nor adherent, further exposing other refractories to oxidation. Porosities form in this outer scale when

there is an enrichment of Mo due to MoO_3 vapor; Cracks and spallation occur likely when there is W or Ta oxides present due to coefficient of thermal expansion mismatch.

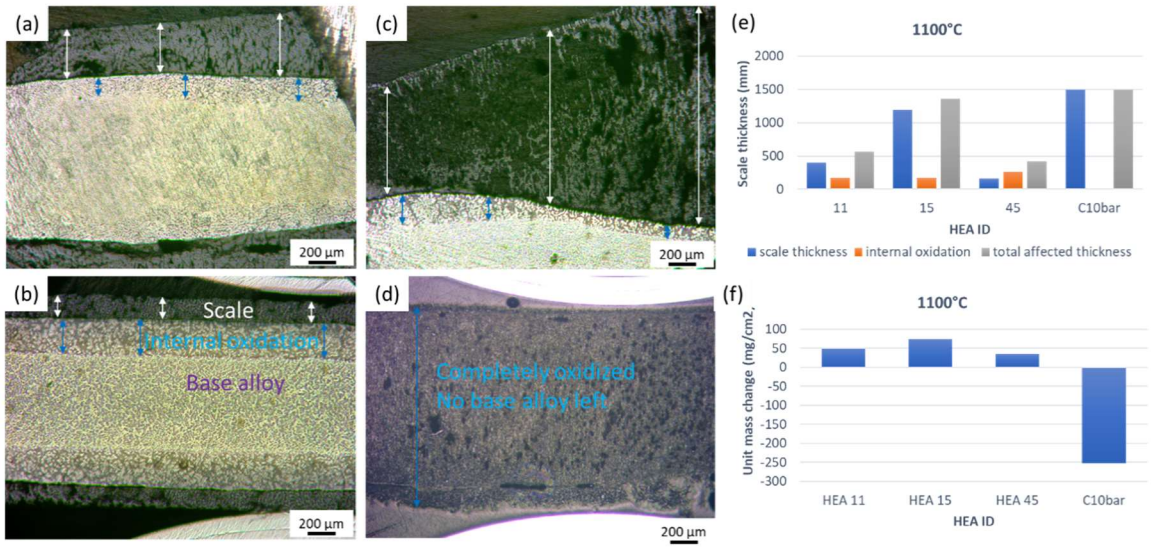

Figure 15. Cross-sectional images of 1373 K 1hour oxidized samples of (a) HEA11; (b) HEA15; (c) HEA45; (d) **C$\overline{10}$** with (e) a chart of the scale thickness, and (f) their mass changes, showing the difference in oxidation behavior determined experimentally.

Though not dense, the thick outer oxide scale serves as a barrier for oxygen transport, lowing the oxygen partial pressure to a level that only interdendritic Zr and Ti are oxidized, forming the internal oxidation zone. HEA45 has more Zr but less W with the same level of Ta compared to HEA15. Of our four selected HEAs from high, medium, and low AUC2 regions, HEA45 showed better oxidation resistance over HEA11, HEA15, and C$\overline{10}$; suggesting that while the thermodynamic favorability of the base alloy is important, the presence of Tungsten-oxides acclerates the corrision process (greater relative levels of Zr than levels of W are beneficial in improving oxidation resistance).

Unfortunately, HEA15 does not fully adhere to our prediction as it has worsened oxidation behavior than HEA11 despite having greater amounts Zr (20% vs 10%) and lesser amounts W (20% vs 30%). Experimentally, this could be purely due to a microstructure effect (not included in this study). The interdendritic region that was preferably oxidized and the porosity left by MoO_3 may have exceeded the percolation threshold forming interconnected channels for easy oxygen pathway for HEA15. We also want to highlight that it is critical to allow slow oxidation in order to relieve the internal stresses, however, the Ta_2O_5 should be avoided as much as possible for improved oxidation. A final conjecture is the continuation of the previously alluded to methodology that utilizes the Pilling-Bedford Ratio (PBR) and Lack of

Monotonicity (LOM) calculations. This theory will justify the experimentally observed trend and explain the effects of oxide decomposition biproducts on oxidation resistance.

Pilling-Bedford Ratio (PBR) and Lack of Monotonicity (LOM)*:* We have already established that increasing amounts of oxygen results in greater phase fractional amounts of oxides due to increased exposure to static oxygen. Notably, the oxidation resistance is dependent on the "quality" of the oxide scales that form. The Pilling-Bedford Ratio (PBR) quantifies the scale quality by comparing the molar volumes of the oxides to the molar volume of the base alloy. The change in the PBR as function of oxygen content is shown in **Figure 16**.

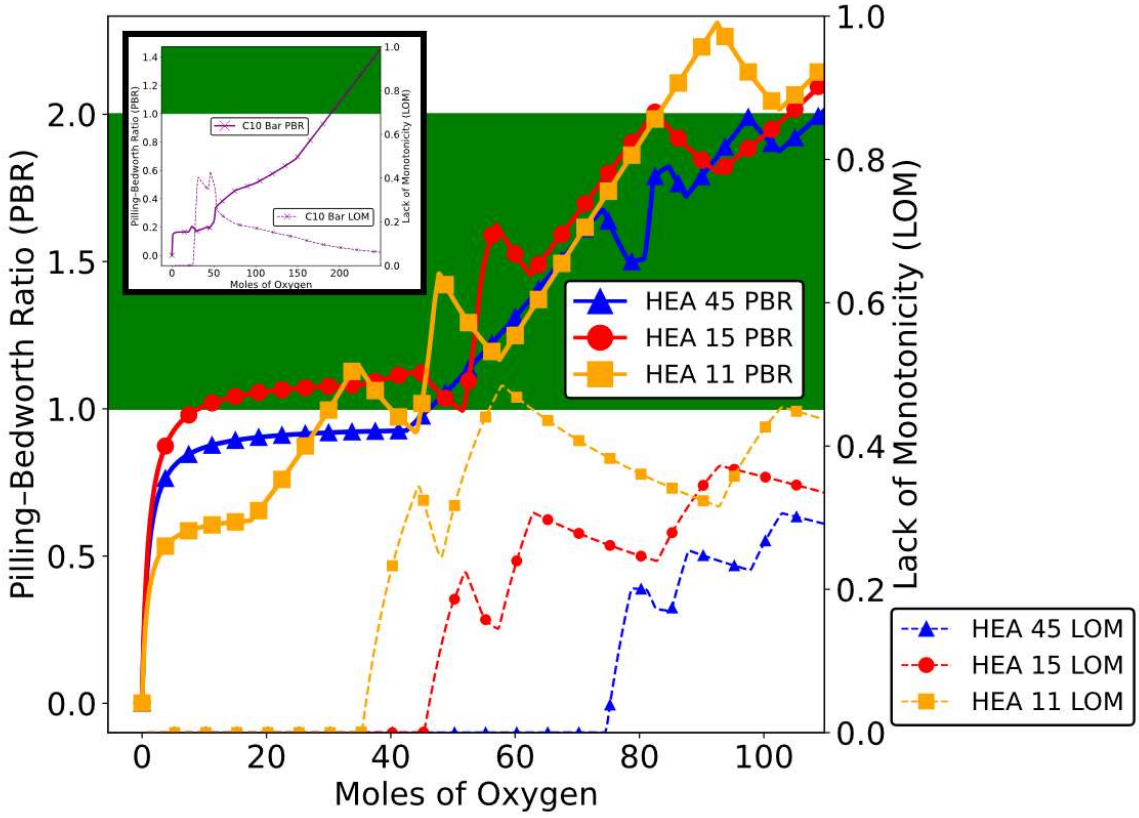

Figure 16. The change of PBR of HEA45, HEA15, and HEA11 at 1373 K. The green region from 1.0 to 2.0 is the ideal PBR value. In addition, we calculate the normalized LOM trends from PBR (see right axis bar). The inset depicts the same information for the C$\overline{\mathbf{10}}$ MPEA from Ref. 22.

The diagram can effectively be evaluated in three regions each of which illustrates several effects contributing or detracting from general oxidation resistance. Up to 40 moles of oxygen we observe a continuous volumetric oxide growth for alloys HEA45, HEA15, and HEA11. Additionally, they each fall short or staddle the cutoff of an ideal PBR level. From 40 to roughly 90 moles of oxygen, we continue to see expanding oxide growth, however this growth is volumetrically volatile.

In the previous region the LOM values were all zero. In this region, the jagged increasing nature of the PBR curve is captured in the non-zero values of the normalized LOM trend. We conjecture that a non-monotonic PBR indicates the existence tensile and compressive stresses between the oxide scale layers that form as oxygen diffuses through the system. Consider that HEA45 is monotonic for a greater amount of molar oxygen. This would indicate that HEA 45 is more mechanically stable than HEA15 and HEA11. From 90 moles of oxygen and beyond the curves breaks out of the ideal PBR region indicating large scales that go through spallation with enough time. Finally, considering the smaller diagram depicting $C\overline{10}$, the PBR falls very far below the ideal PBR limit and is very non-monotonic. This further confirms the very poor oxidation resistance.

Summary and notable considerations in future development and use of the framework: This work establishes the "High-Throughput Finite-temperature Phase Prediction Framework", and its application in predicting the oxidation behavior of RHEAs. The framework itself uses the Bartel prediction model augmented with a short-range ordering Gibbs formation energy. After an elemental reservoir is specified, this prediction model is used on the combined with user databases. Subsequently, the framework selects phases that results in a minimum solid-solution energy followed by energy minimization using grand canonical linear programming method that determines the change in resulting elemental chemical potential of RHEAs. We are aware the external conditions can be used for multiphase formation such as cooling rate (61), however, this work considers single phase RHEAs for high-throughput assessment of phase stability and oxidation behavior.

For a practical application, a database of 51 HEA crystal structures of Mo-Ta-Ti-W-Zr phase spaces were iteratively combined with the OQMD subset and incrementally increased in temperature and oxygen content to observe the thermodynamic oxidation behavior. Using AUC2 scores, it was determined that greater concentrations of Tungsten and Tantalum are responsible for diminished returns of HEA formation as they are exposed to oxygen. Additionally, from the AUC2 scores of the decomposing phases, a trend of the oxide formations was determined based on the aggregate scores of the all the HEAs. Using literature experimental results, a rule-of-thumb selection criteria, in place of kinetic calculations, was created to justify the maximization or minimization of particular oxides for a desirable oxidation behavior.

To experimentally validated our predictions, we chose three composition HEA15, HEA45, and HEA11 including one independent RHEA, i.e., $C\overline{10}$, which is known to perform badly during oxidation. Experiments found HEA15 perform rather poorly, therefore, remained an outlier compared to both HEA45 and HEA11. This warranted a more encompassing theory to rationalize our predictions. Thus, we

implemented an analysis based on Pilling-Bedford Ratio (PBR) and Lack of Monotonicity (LOM) values which provide in depth understanding of disparity between theory and experiments.

To conclude, the entire sequence of analysis that emphasizes the thermodynamic stability of HEA formation and optimizing the oxidation selection, there are some notable considerations that should be discussed for completeness. Some realistic and more advanced considerations such as evaporation and sublimation in HEA oxidation are not addressed in this work, which needs model correction for the given properties in our future developments that will set line-item rules for eliminating or penalizing certain phases from forming at higher temperature, for example, MoO_3 evaporates at fairly low temperatures (1068 K) (62) while WO_3 and Ta_2O_5 evaporates above 1273 K (62) and 1643 K (62). The remaining caveats of AUC2 localization and kinetic considerations have been discussed, however, for the purposes of best practices it may be more advantageous to bifurcate the study in future into two temperature domains or narrow the temperature range to a specific region of interest.

A final note is that oxidation characterization and prediction extremely difficult. Considering that our phase space is five component system it is a highly non-linear processes with multiple levels of physics all competing and complementing each other while dividing up the limited amount of oxygen provided. Our objective was to create a rapid means of determining oxidation paths. While our framework has yet to be exhaustively tested, it provides a sound starting point for the rapid screening for oxidation resistance in complex alloys. Combined computational & experimental studies may also make the screening more robust against lack of theoretical analysis of kinetic and/or microstructural effects.

Acknowledgements: ARPA-E ULTIMATE project Batch-wise Improvement in Reduced Design Space using a Holistic Optimization Technique (BIRDSHOT) under primary contract No. DE-AR0001427 is acknowledged. RA acknowledge the support of QNRF under Project No. NPRP11S-1203-170056. DS acknowledges the support of NSF through Grant No. NSF-DGE-1545403. The work at Ames Laboratory was supported by U.S. Department of Energy (DOE), Office of Science, Basic Energy Sciences, Materials Science & Engineering Division. Ames Laboratory operated by Iowa State University for the U.S. DOE under contract DE-AC02-07CH11358. This work was also supported in part (experimental oxidation studies) by the DOE-FE (AMR program) through Ames Laboratory contract no.DE-AC02-07CH11358. Calculations were conducted using the advanced computing resources provided by Texas A&M High-Performance Research Computing.

Supplementary Information (SI)

Supplementary Information Document

Supplementary Data 1: Bartel Predictions of OQMD and HEA Dataset

Supplementary Data 2: Ground-state HEA Data

Supplementary Data 3: HEA and phases AUC2 scores

Supplementary Data Collection 1: HEA Phase Fraction Prediction

Supplementary Data Collection 2: HEA Reaction Prediction

Supplementary Data Collection 3: HEA Chemical Potentials

Data Availability Statement: The code and data will be made available from the corresponding author upon reasonable request.

Competing interests: The authors declare no competing financial interests.

Conflicts interest: There are no conflicts to declare.

Correspondence: DS (danielsauceda@tamu.edu), PS (psingh84@ameslab.gov) or RA (raymundo.arroyave@tamu.edu).

References

1. Müller F, Gorr B, Christ H-J, Müller J, Butz B, Chen H, et al. On the oxidation mechanism of refractory high entropy alloys. Corrosion Science. 2019;159:108161.
2. Marques F, Balcerzak M, Winkelmann F, Zepon G, Felderhoff M. Review and outlook on high-entropy alloys for hydrogen storage. Energy & Environmental Science. 2021;14(10):5191-227.
3. Gorr B, Schellert S, Müller F, Christ H-J, Kauffmann A, Heilmaier M. Current Status of Research on the Oxidation Behavior of Refractory High Entropy Alloys. Advanced Engineering Materials. 2021;23(5):2001047.
4. Ma Y, Ma Y, Wang Q, Schweidler S, Botros M, Fu T, et al. High-entropy energy materials: challenges and new opportunities. Energy & Environmental Science. 2021;14(5):2883-905.
5. Senkov ON, Miracle DB, Chaput KJ, Couzinie J-P. Development and exploration of refractory high entropy alloys—A review. Journal of Materials Research. 2018;33(19):3092-128.
6. Gorr B, Mueller F, Christ HJ, Mueller T, Chen H, Kauffmann A, et al. High temperature oxidation behavior of an equimolar refractory metal-based alloy 20Nb 20Mo 20Cr 20Ti 20Al with and without Si addition. Journal of Alloys and Compounds. 2016;688:468-77.

7. Gorr B, Müller F, Azim M, Christ H-J, Müller T, Chen H, et al. High-Temperature Oxidation Behavior of Refractory High-Entropy Alloys: Effect of Alloy Composition. Oxidation of Metals. 2017;88(3-4):339-49.
8. Müller F, Gorr B, Christ H-J, Chen H, Kauffmann A, Heilmaier M. Effect of microalloying with silicon on high temperature oxidation resistance of novel refractory high-entropy alloy Ta-Mo-Cr-Ti-Al. Materials at High Temperatures. 2017;35(1-3):168-76.
9. Tolpygo VK, Dryden JR, Clarke DR. Determination of the growth stress and strain in α-Al2O3 scales during the oxidation of Fe–22Cr–4.8Al–0.3Y alloy. Acta Materialia. 1998;46(3):927-37.
10. Tolpygo VK, Clarke DR. Competition Between Stress Generation and Relaxation During Oxidation of an Fe-Cr-Al-Y Alloy. Oxidation of Metals. 1998;49(1/2):187-212.
11. Huntz AM. Stresses in NiO, Cr2O3 and Al2O3 oxide scales. Materials Science and Engineering: A. 1995;201(1-2):211-28.
12. Gao MC, Yeh J-W, Liaw PK, Zhang Y. High-Entropy Alloys2016.
13. Shi Y, Yang B, Liaw P. Corrosion-Resistant High-Entropy Alloys: A Review. Metals. 2017;7(2):43.
14. Miracle DB, Senkov ON. A critical review of high entropy alloys and related concepts. Acta Materialia. 2017;122:448-511.
15. Ostovari Moghaddam A, Shaburova NA, Samodurova MN, Abdollahzadeh A, Trofimov EA. Additive manufacturing of high entropy alloys: A practical review. Journal of Materials Science & Technology. 2021;77:131-62.
16. Ostovari Moghaddam A, Trofimov EA. Toward expanding the realm of high entropy materials to platinum group metals: A review. Journal of Alloys and Compounds. 2021;851:156838.
17. Chen J, Zhou X, Wang W, Liu B, Lv Y, Yang W, et al. A review on fundamental of high entropy alloys with promising high–temperature properties. Journal of Alloys and Compounds. 2018;760:15-30.
18. Saunders SRJ, Nicholls JR. Oxidation, Hot Corrosion and Protection of Metallic Materials. In: Cahn RW, Hassen P, Eds., editors. Physical Metallurgy. 4th ed1996. p. 1291-361.

19. Stratton P. Ellingham diagrams – their use and misuse. Heat Treatment and Surface Engineering. 2013;7(2):70-3.
20. Dove MT. Introduction to Lattice Dynamics2010.
21. Singh P, Smirnov AV, Johnson DD. Atomic short-range order and incipient long-range order in high-entropy alloys. Physical Review B. 2015;91(22):224204.
22. Singh P, Sharma A, Smirnov AV, Diallo MS, Ray PK, Balasubramanian G, et al. Design of high-strength refractory complex solid-solution alloys. npj Computational Materials. 2018;4(1):16.
23. Zhang R, Zhao S, Ding J, Chong Y, Jia T, Ophus C, et al. Short-range order and its impact on the CrCoNi medium-entropy alloy. Nature. 2020;581(7808):283-7.
24. Sundman B, Fries SG, Oates WA. A thermodynamic assessment of the Au-Cu system. Calphad. 1998;22(3):335-54.
25. Bartel CJ, Millican SL, Deml AM, Rumptz JR, Tumas W, Weimer AW, et al. Physical descriptor for the Gibbs energy of inorganic crystalline solids and temperature-dependent materials chemistry. Nat Commun. 2018;9(1):4168.
26. Sauceda D, Singh P, Falkowski AR, Chen Y, Doung T, Vazquez G, et al. High-throughput reaction engineering to assess the oxidation stability of MAX phases. npj Computational Materials. 2021;7(1):6.
27. R. Akbarzadeh A, Ozoliņš V, Wolverton C. First-Principles Determination of Multicomponent Hydride Phase Diagrams: Application to the Li-Mg-N-H System. Advanced Materials. 2007;19(20):3233-9.
28. Kirklin S, Meredig B, Wolverton C. High-Throughput Computational Screening of New Li-Ion Battery Anode Materials. Advanced Energy Materials. 2013;3(2):252-62.
29. Ogura M, Fukushima T, Zeller R, Dederichs PH. Structure of the high-entropy alloy Al CrFeCoNi: fcc versus bcc. Journal of Alloys and Compounds. 2017;715:454-9.
30. Schliephake D, Azim M, von Klinski-Wetzel K, Gorr B, Christ H-J, Bei H, et al. High-Temperature Creep and Oxidation Behavior of Mo-Si-B

Alloys with High Ti Contents. Metallurgical and Materials Transactions A. 2013;45(3):1102-11.
31. Azimovna Azim M, Burk S, Gorr B, Christ H-J, Schliephake D, Heilmaier M, et al. Effect of Ti (Macro-) Alloying on the High-Temperature Oxidation Behavior of Ternary Mo–Si–B Alloys at 820–1,300 °C. Oxidation of Metals. 2013;80(3-4):231-42.
32. Vazquez A, Varma SK. High-temperature oxidation behavior of Nb–Si–Cr alloys with Hf additions. Journal of Alloys and Compounds. 2011;509(25):7027-33.
33. Xu C, Gao W. Pilling-Bedworth ratio for oxidation of alloys. Materials Research Innovations. 2016;3(4):231-5.
34. Kirklin S, Saal JE, Meredig B, Thompson A, Doak JW, Aykol M, et al. The Open Quantum Materials Database (OQMD): assessing the accuracy of DFT formation energies. npj Computational Materials. 2015;1(1):15010.
35. Jain A, Ong SP, Hautier G, Chen W, Richards WD, Dacek S, et al. Commentary: The Materials Project: A materials genome approach to accelerating materials innovation. APL Materials. 2013;1(1):011002.
36. van de Walle A, Asta M, Ceder G. The alloy theoretic automated toolkit: A user guide. Calphad. 2002;26(4):539-53.
37. van de Walle A, Tiwary P, de Jong M, Olmsted DL, Asta M, Dick A, et al. Efficient stochastic generation of special quasirandom structures. Calphad. 2013;42:13-8.
38. van de Walle A. Multicomponent multisublattice alloys, nonconfigurational entropy and other additions to the Alloy Theoretic Automated Toolkit. Calphad. 2009;33(2):266-78.
39. Perdew JP, Burke K, Ernzerhof M. Generalized Gradient Approximation Made Simple. Phys Rev Lett. 1996;77(18):3865-8.
40. Kresse G, Furthmuller J. Efficient iterative schemes for ab initio total-energy calculations using a plane-wave basis set. Phys Rev B Condens Matter. 1996;54(16):11169-86.

41. Kresse G, Furthmüller J. Efficiency of ab-initio total energy calculations for metals and semiconductors using a plane-wave basis set. Computational Materials Science. 1996;6(1):15-50.
42. Kresse G, Hafner J. Ab initio molecular-dynamics simulation of the liquid-metal-amorphous-semiconductor transition in germanium. Phys Rev B Condens Matter. 1994;49(20):14251-69.
43. Kresse G. Ab initio molecular dynamics for liquid metals. Journal of Non-Crystalline Solids. 1995;192-193:222-9.
44. Monkhorst HJ, Pack JD. Special points for Brillouin-zone integrations. Physical Review B. 1976;13(12):5188-92.
45. Arroyave R, Shin D, Liu ZK. Ab initio thermodynamic properties of stoichiometric phases in the Ni–Al system. Acta Materialia. 2005;53(6):1809-19.
46. Mandl F. Statistical Physics: Wiley; 1971. 224 p.
47. Andersson JO, Guillermet AF, Hillert M, Jansson B, Sundman B. A compound-energy model of ordering in a phase with sites of different coordination numbers. Acta Metallurgica. 1986;34(3):437-45.
48. Davydov Y, Zitikis R. Quantifying non-monotonicity of functions and the lack of positivity in signed measures. Modern Stochastics: Theory and Applications. 2017;4(3):219-31.
49. Kofstad P. High Temperature Oxidation of Metals1966.
50. Cao Y-k, Liu Y, Liu B, Zhang W-d, Wang J-w, Du M. Effects of Al and Mo on high temperature oxidation behavior of refractory high entropy alloys. Transactions of Nonferrous Metals Society of China. 2019;29(7):1476-83.
51. Senkov ON, Senkova SV, Dimiduk DM, Woodward C, Miracle DB. Oxidation behavior of a refractory NbCrMo0.5Ta0.5TiZr alloy. Journal of Materials Science. 2012;47(18):6522-34.
52. Cramer SDCJ, Bernard S

Moosbrugger, Charles. ASM handbook volume 13b: corrosion: materials: Asm International; 2005.

53. Butler TM, Chaput KJ. Native oxidation resistance of Al20Nb30Ta10Ti30Zr10 refractory complex concentrated alloy (RCCA). Journal of Alloys and Compounds. 2019;787:606-17.
54. Ostrovskaya O, Badini C, Baudana G, Padovano E, Biamino S. Thermogravimetric investigation on oxidation kinetics of complex Ti-Al alloys. Intermetallics. 2018;93:244-50.
55. Li L-C, Li M-X, Liu M, Sun B-Y, Wang C, Huo J-T, et al. Enhanced oxidation resistance of MoTaTiCrAl high entropy alloys by removal of Al. Science China Materials. 2020;64(1):223-31.
56. Birks N, Meier GH, Pettit FS. Introduction to the High-Temperature Oxidation of Metals2006.
57. Sheikh S, Bijaksana MK, Motallebzadeh A, Shafeie S, Lozinko A, Gan L, et al. Accelerated oxidation in ductile refractory high-entropy alloys. Intermetallics. 2018;97:58-66.
58. Wang F, Northwood DO. Oxides formed between ZrO2 and Nb2O5. Journal of Materials Science. 2004;30(16):4003-8.
59. Savitskii EM, Burkhanov GS. Physical Metallurgy of Refractory Metals and Alloys1995.
60. Su R, Zhang H, Ouyang G, Liu L, Nachlas W, Cui J, et al. Enhanced oxidation resistance of (Mo95W5)85Ta10(TiZr)5 refractory multi-principal element alloy up to 1300°C. Acta Materialia. 2021;215.
61. Li J, Xie B, Li L, Liu B, Liu Y, Shaysultanov D, et al. Performance-oriented multistage design for multi-principal element alloys with low cost yet high efficiency. Mater Horiz. 2022;9(5):1518-25.
62. Tietz TEW, Jess W. Behavior and properties of refractory metals: Stanford University Press; 1965.